Quantum Entanglement Phase Transitions and Computational Complexity: Insights from Ising Models

Hanchen Liu,[*] Vikram Ravindranath, and Xiao Chen[†]

Department of Physics, Boston College, Chestnut Hill, Massachusetts 02467, USA

(Dated: August 19, 2023)

In this paper, we construct 2-dimensional bipartite graph states and perform single-qubit measurements on the bulk qubits. We explore the entanglement scaling of the unmeasured 1-dimensional boundary state and show that under certain conditions, the boundary state can undergo a volume-law to an area-law entanglement transition driven by variations in the measurement angle. We bridge this boundary state entanglement transition and the measurement induced phase transition in the non-unitary 1+1-dimensional circuit via the transfer matrix method. We also explore the application of this entanglement transition on the computational complexity problems. Specifically, we establish a relation between the boundary state entanglement transition and the sampling complexity of the bipartite 2d graph state, which is directly related to the computational complexity of the corresponding Ising partition function with complex parameters. By examining the boundary state entanglement scaling, we numerically identify the parameter regime for which the 2d quantum state can be efficiently sampled, and in such region the Ising partition function can be approximately evaluated efficiently.

CONTENTS

* hanchen.liu@bc.edu
† chenaad@bc.edu; Department of Physics, Boston College, Chestnut Hill, Massachusetts 02467, USA

I. INTRODUCTION

Measurement-induced entanglement phase transitions (MIPT) have been the subject of extensive research in the scientific community. Numerous studies have explored these transitions in various quantum systems, investigating their fundamental properties and experimental realization [1–6]. One type of phase transition exists in the hybrid quantum circuit. By tuning the measurement rate, there exists an entanglement transition from the volume-law phase to the area-law phase [1, 2]. Another example of entanglement phase transitions occurs in measurement-only circuit systems, where the transition is between different area-law phases, with a deviation from area-law scaling at the critical point [6–9]. An illustrative example of such a system is the ZZ/X competing measurement model present in [3], whose transition can be understood in the context of classical percolation.

The entanglement structure of a quantum system plays a crucial role in determining the computational difficulty of simulating the system on a classical computer. Simulating a volume-law entangled system is widely recognized as challenging due to the exponential resources required to store the quantum state. Conversely, an area-law entangled system is easily simulatable, as demonstrated by the matrix product state (MPS) representation and tensor networks, along with their variants [10]. Therefore, MIPT in the 1+1d hybrid quantum circuit naturally implies a complexity phase transition in terms of simulability.

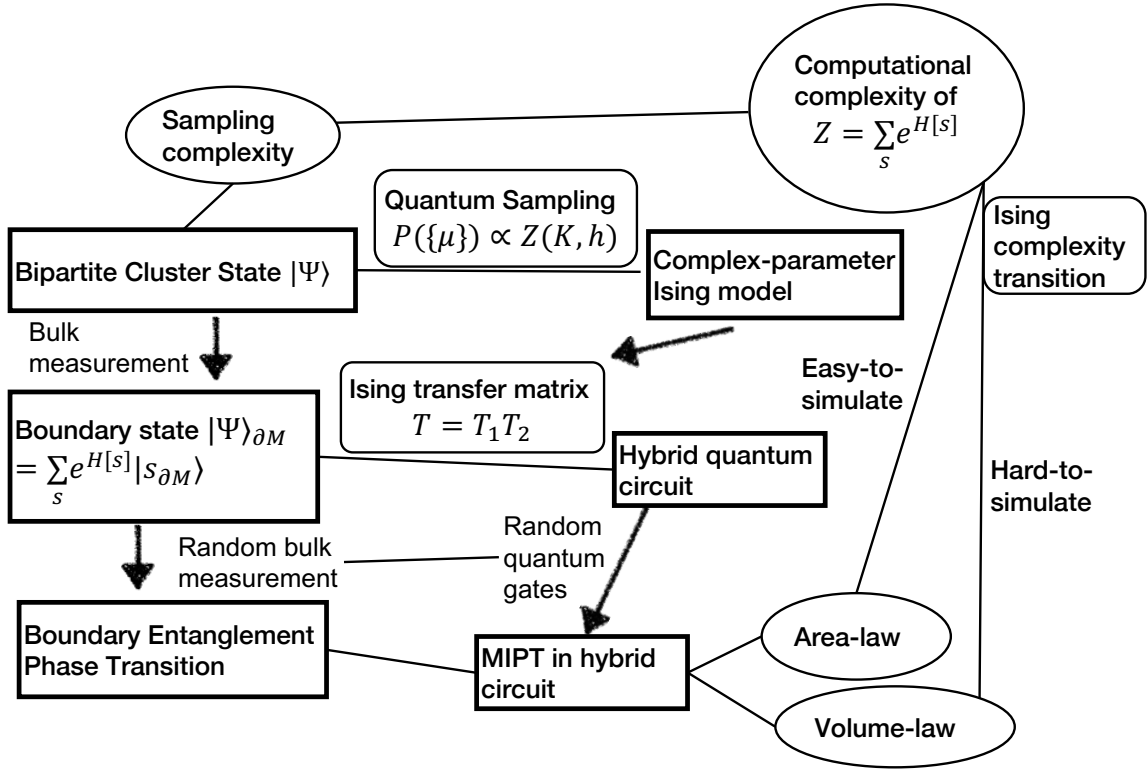In addition to this, MIPT exhibits interesting connec-

FIG. 1. Road map of this work

.

tions with other computational problems. For example, in the context of the 2d shallow circuit sampling problem [6, 11–13], it is known that exact classical sampling of the outcome of a 2d shallow circuit on a classical computer is generally challenging. However, approximate sampling becomes feasible for circuits with small depths $d \leq d_c$, where d_c is some finite critical circuit depth [6]. Conversely, as the circuit depth exceeds d_c, approximate sampling of such systems becomes computationally difficult. The connection to 1+1d MIPT can be understood by treating one spatial dimension as the time direction and interpreting the circuit depth as the inverse of the measurement rate. Consequently, the complexity transition observed in 2d shallow circuit sampling is equivalent to 1+1d MIPT.

Motivated by these advancements, in our recent work [11], we explicitly consider 2d quantum states generated by various Clifford shallow circuits. We then investigate the entanglement structure of the unmeasured boundary 1d quantum state by measuring all the bulk qubits. Remarkably, we demonstrate that in various shallow circuits, this boundary state undergoes a volume-law to area-law entanglement phase transition. Similar ideas were also discussed in Ref. 12. To illustrate this, we focus on a graph state generated on a square lattice and employ random single qubit X or Z measurements for the bulk qubits. Our findings reveal that by manipulating the ratio between X and Z measurements, the bound-

ary 1d state undergoes the volume-law to the area-law entanglement transition.

In this paper, we aim to gain a deeper understanding of the boundary entanglement phase transition in various 2d graph states and its connection with transitions in computational complexity. To achieve this objective, we take the following three approaches: (1) We establish a connection between the sampling problem of the 2d graph state defined on the bipartite lattice and the Ising partition function with complex parameters. (2) We reveal that the 1d boundary state carries essential information about the 2d bulk Ising partition function. Employing the transfer matrix approach, we also illustrate that the boundary state can be generated through 1+1d non-unitary dynamics. (3) We undertake numerical evaluations of the entanglement entropy of the 1d boundary state by performing single qubit measurements for the bulk qubits. We observe and analyze various entanglement phase transitions by varying the measurement angle on the Bloch sphere or the ratio between X/Y/Z Pauli measurements. Through these three approaches, we effectively demonstrate that the boundary entanglement transition in the graph state is closely linked to the complexity transition of the 2d Ising models. Specifically, in the volume-law phase, the corresponding 2d Ising partition function is challenging to evaluate, while in the area-law phase, the corresponding 2d Ising partition function becomes easy to evaluate. Our findings shed light on

the intricate interplay between boundary entanglement scaling and computational complexity and demonstrate the (im)-possibility of efficient classical approximations of Ising models with complex parameters. A road map of this work is shown in Fig. 1.

II. RESOURCE STATE SAMPLING PROBLEM

In this section, we will examine the relationship between the toric code, cluster state, and the classical Ising partition function, following similar steps as outlined in previous works [14, 15]. We first introduce the measurement basis

$$\mathcal{B}(w) = \{|\mu, w\rangle \equiv \bigotimes_{i \in \Lambda} |\mu_i, w_i\rangle_i \mid \mu_i \in \mathbb{Z}_2\} \quad (1)$$

where Λ is the set of all qubits, $w \equiv \{w_i\} \in \mathbb{C}^{|\Lambda|}$ labels the measurement direction configuration, $\mu \equiv \{\mu_i\} \in \mathbb{Z}_2^{|\Lambda|}$ is the measurement outcome configuration, and $|\ldots\rangle_i$ is the quantum state defined on local Hilbert space of qubit i.

The local projective measurement on qubit i along $\hat{O}_i = \cos\theta_i Z_i + \sin\theta_i \cos\varphi_i X_i + \sin\theta_i \sin\varphi_i Y_i$, where (θ_i, φ_i) is given by the standard definition of spherical coordinates, collapses the single-site wave function on qubit i to a measurement state

$$|+, (\theta_i, \varphi_i)\rangle_i = \cos\frac{\theta_i}{2} |0\rangle_i + \exp(i\varphi_i)\sin\frac{\theta}{2} |1\rangle_i$$
$$|-, (\theta_i, \varphi_i)\rangle_i = \sin\frac{\theta_i}{2} |0\rangle_i - \exp(i\varphi_i)\cos\frac{\theta}{2} |1\rangle_i \quad (2)$$

where $|0\rangle_i$ and $|1\rangle_i$ are the eigenstates of Pauli Z on qubit i, that satisfy $Z_i |0\rangle_i = |0\rangle_i$, $Z_i |1\rangle_i = -|1\rangle_i$. We define

$$w_i \equiv \tan(\theta_i/2)\exp(i\varphi_i), \quad (3)$$

and then introduce the weight parameter W_i

$$W_i \equiv \begin{cases} w_i & \text{if } \mu = +1 \\ -[(w_i)^*]^{-1} & \text{if } \mu = -1 \end{cases}, \quad (4)$$

where $(\cdots)^*$ is the complex conjugate. The measurement state is further written more compactly as

$$|\mu_i, w_i\rangle_i = N_i (|0\rangle_i + W_i |1\rangle_i) \quad (5)$$

where $N_i = 1/\sqrt{1 + |W_i|^2}$ is the normalization factor, w_i is the measurement direction parameter defined in Eq. 3, and μ is the measurement outcome. It is easy to show that for a given measurement direction configuration $\{\theta_i, \varphi_i\}$, the set of measurement states $\{\bigotimes_{i \in \Lambda} |\mu_i, w_i\rangle_i, \mu_i = \pm 1\}$ form a complete basis $\mathcal{B}(w)$ of the Hilbert space of given by qubit set Λ, and we define such basis to be the measurement basis.

We now try to expand a multi-qubit wave function $|\Psi\rangle$ in the measurement basis. Formally, it can be written as

$$|\Psi\rangle = \sum_{\mu} \Omega_{w,\mu} |\mu, w\rangle, \quad (6)$$

where $\Omega_{w,\mu} = \langle \mu, w |\Psi\rangle$ is the overlap between measurement base state $|\mu, w\rangle \in \mathcal{B}$ and the multi-qubit wave function $|\Psi\rangle$. The summation is over all the allowed measurement outcome configurations μ. We will show later in this section that the overlap function can be written in the form of the partition function of classical spin systems

$$\Omega_{w,\mu} \propto \mathcal{Z}(K, h). \quad (7)$$

with the effective coupling K and effective magnetic field h being functions of the measurement outcome μ, and measurement direction ω. Calculating such overlap function is essential in quantum sampling problems, which is commonly used as a demonstration of quantum advantage.

A. The toric code state

The toric code state gives a simple example. The toric code state, as first introduced in [16], is the ground state of the Hamiltonian given by

$$H = -\sum_v A_v - \sum_p B_p, \quad (8)$$

where the qubits are defined on the edges of a square lattice. Here, $A_v = \prod_{i \in v} X_i$ represents the vertex operator, which is the product of Pauli X operators enclosing the vertex v, and $B_p = \prod_{j \in p} Z_j$ represents the plaquette operator, which is the product of Pauli Z operators associated with the plaquettes p. The ground state of such a Hamiltonian takes the form

$$|\Psi\rangle^{TC} = \frac{1}{|\mathcal{C}|} \sum_{l \in \mathcal{C}} |l\rangle, \quad (9)$$

where $\mathcal{C}$ is the set of configurations of closed loops formed by connecting edges on the dual lattice, $|\mathcal{C}|$ is the number of the loops, and $|l\rangle$ is the quantum state related to such loop configuration $l \in \mathcal{C}$. The explicit form of $|l\rangle$ is

$$|l\rangle = \bigotimes_{i \in l, j \notin l} |1\rangle_i \otimes |0\rangle_j. \quad (10)$$

An example of such a loop is shown in Figure. 2.

We now calculate the overlap function $\Omega_{w,\mu}$ for the toric code state. Utilizing Eq. (5), we can demonstrate that the overlap function is given by:

$$\Omega_{w,\mu} = \frac{\prod_i N_i}{|\mathcal{C}|} \sum_{l \in \mathcal{C}} W_l. \quad (11)$$

Each loop configuration takes a weight of $W_l = \prod_{i \in l} W_i$ that can be effectively treated as the Boltzmann weight for a domain wall configuration in the Ising model. The overlap function is thus

$$\Omega_{w,\mu} \propto \sum_s \exp\left(\sum_{i = \langle k, l \rangle} K_i s_k s_l\right), \quad (12)$$
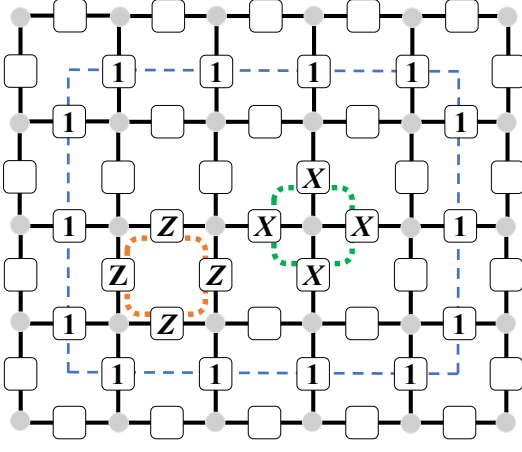
FIG. 2. Toric code conventions: green dashed line represents the vertex operator A_v, the orange dashed line represents the plaquette operator B_p, and the blue dashed line gives an example of the quantum state related to closed-loop l.

where

$$\exp(-2K_i) = W_i, \tag{13}$$

with $i = \langle k, l \rangle$ being the edge connecting site neighboring site k and l and the classical spins $\{s\}$ are defined on the vertices of the square lattice given in Fig. 2.

B. The bipartite cluster state

We now consider cluster states defined on bipartite graphs. The cluster state is a stabilizer state defined on a graph $G = (V, E)$, where the stabilizer generator takes the form

$$g_i = X_i \prod_{j \in \mathcal{N}_i} Z_j \quad i \in V. \tag{14}$$

where $j \in \mathcal{N}_i$ is the neighbor of vertex i, and the cluster state $|\Psi\rangle$ satisfies the stabilizer condition $g_i |\Psi\rangle = |\Psi\rangle$, for all $i \in V$. For a bipartite graph G, the stabilizer generators naturally split into two sets:

$$\begin{aligned} g_i &= X_i \prod_{j \in \mathcal{N}_i} Z_j \quad \text{for } i \in \circ \\ g_m &= X_m \prod_{n \in \mathcal{N}_m} Z_n \quad \text{for } m \in \bullet, \end{aligned} \tag{15}$$

where $\mathcal{N}_{i/m}$ denotes the neighbors of site i/m, and $\circ, \bullet \subset V$ labels the bipartition of graph vertices. Two examples of graph bipartition are shown in Fig. 7.

Applying Hardmard rotation H on the $\bullet \in V$ sites of the bipartite graph state, we have the hardmard rotated state $|\Psi\rangle_H = \prod_{i \in \bullet} H_i |\Psi\rangle$, which is stabilized under

$$\begin{aligned} g_i^X &= X_i \prod_{j \in \mathcal{N}_i} X_j \quad \text{for } i \in \circ \\ g_m^Z &= Z_m \prod_{n \in \mathcal{N}_m} Z_n \quad \text{for } m \in \bullet, \end{aligned} \tag{16}$$
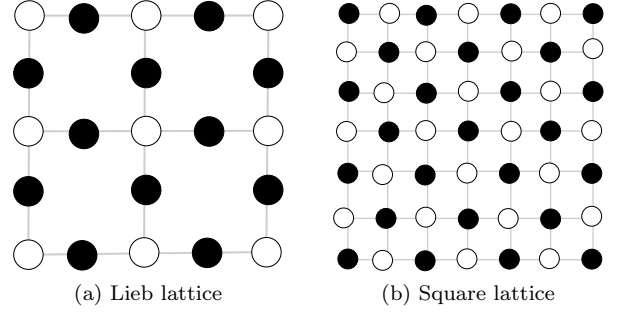

(a) Lieb lattice   (b) Square lattice

FIG. 3. Lattice bipartitions

as presented in [15]. The rotated quantum state $|\Psi\rangle_H$ can then be expressed as

$$\begin{aligned} |\Psi\rangle_H &= \frac{1}{2^N} \prod_{m \in \bullet} (1 + g_m^Z) \prod_{i \in \circ} (1 + g_i^X) \bigotimes_{k \in \Lambda} |0\rangle_k \\ &= \frac{1}{2^{|\circ|}} \prod_{i \in \circ} (1 + g_i^X) \bigotimes_{k \in \Lambda} |0\rangle_k \\ &= \frac{1}{2^{|\circ|}} \sum_A g_A^X \bigotimes_{k \in \Lambda} |0\rangle_k \end{aligned} \tag{17}$$

where $\bigotimes_{k \in \Lambda} |0\rangle_k$ is the tensor product of $|0\rangle$'s on all qubits, $g_A^X = \prod_{i \in A_\circ} g_i^X$ is the product of g^X's inside domain A, and $|\circ|$ denotes numbers of $\circ$ qubits.

g_i^X is a star-shaped product of Pauli X's, which means that it contains one Pauli X on the centering site $i \in \circ$ and other Pauli X's on the neighboring sites $j \in \mathcal{N}_i \subset \bullet$. Thus, in $g_A^X = \prod_{i \in A_\circ} g_i^X$, the X_j, $j \in A_\bullet$, inside domain A is canceled, leaving only Pauli X's located at the boundary $\partial A_\bullet$. We may thus write

$$g_A^X = \prod_{i \in A_\circ} X_i \prod_{j \in \partial A_\bullet} X_j, \tag{18}$$

the wave function is therefore of the form

$$|\Psi\rangle_H = \frac{1}{2^{|\circ|}} \sum_A |A\rangle \otimes |\partial A\rangle \otimes |\overline{A}\rangle \tag{19}$$

where A labels the domain configuration determined by whether site $i \in \circ$ is occupied by g_i^X or not. The first $|A\rangle = \bigotimes_{i \in A_\circ} |1\rangle_i$ is the contribution from $\prod_{i \in A_\circ} X \bigotimes_{k \in \Lambda} |0\rangle_k$, the second part $|\partial A\rangle = \bigotimes_{j \in \partial A_\bullet} |1\rangle_j$ is from the domain boundary $\prod_{j \in \partial A_\bullet} X_j \bigotimes_{k \in \Lambda} |0\rangle_k$, and $|\overline{A}\rangle = \bigotimes_{k \notin A} |0\rangle_k$ is from the $|0\rangle_i$'s that are not flipped by g_A^X. One example of the wave function support on Lieb lattice is shown in Fig. 4. The overlap function thus contains two non-trivial contributions W_A and $W_{\partial A}$

$$\Omega_{w,\mu} \propto \sum_A W_A \times W_{\partial A} \tag{20}$$

where

$$W_A = \langle \mu_{A_\bullet}, w_{A_\bullet} | A \rangle = \prod_{i \in A_\bullet} W_i$$

$$W_{\partial A} = \langle \mu_{\partial A_\circ}, w_{\partial A_\circ} | \partial A \rangle = \prod_{i \in \partial A_\circ} W_i$$

with $|\mu_A, w_A\rangle$ and $|\mu_{\partial A_\circ}, w_{\partial A_\circ}\rangle$ being the measurement basis support on $A_\bullet$ and $\partial A_\circ$ are the contributions of the bulk and the boundary of the domain A respectively. When introducing the Ising degrees of freedom $\{s\}$ on $\circ$ sites, W_A can be treated as the onsite magnetic field term whereas the boundary $W_{\partial A}$ contributes to the spin interaction. Thus, the overlap function can be expressed in the form of an Ising partition function,

$$\langle \mu, w | \Psi \rangle_H \propto$$

$$\sum_s \exp\left(\sum_{i \in \bullet} K_i \prod_{j \in \mathcal{N}_i | j \in \circ} s_j + \sum_{k \in \circ} h_k s_k \right). \quad (21)$$

where the classical spins $\{s_i\}$ are defined on the $\circ$ sublattice. The effective multi-spin coupling constant K_i is given by $\exp(-2K_i) = W_i$ with $i \in \bullet$, and the onsite effective magnetic field is obtained from $\exp(-2h_k) = W_k$ with $k \in \circ$. The overlap function of $|\Psi\rangle$ without Hardmard rotation can be obtained using the identity

$$\langle \mu, w | \Psi \rangle = \langle \mu, w | \prod_{i \in \bullet} H_i^\dagger H_i | \Psi \rangle = \langle \mu, w' | \Psi \rangle_H \quad (22)$$

where $W_i' = W_i$ for $i \in \circ$, and $W_i' = (1 - W_i)/(1 + W_i)$ for $i \in \bullet$ due to the Hardmard rotation on site $i \in \bullet$. The correspondence between the measurement parameter $\{W_i, W_k\}$ and the Ising parameters $\{K_i, h_k\}$ are now

$$\begin{aligned} \exp(-2h_k) &= W_k & k \in \circ \\ \exp(-2K_i) &= \frac{1 - W_i}{1 + W_i} & i \in \bullet \end{aligned}. \quad (23)$$

It should be noted that the variable W_i is generally complex, implying that both K_j and h_j can take complex values.

One simple example is the cluster state defined on the Lieb lattice, the bipartition of such lattice is shown in Fig. 3a, where the vertices are labeled "$\circ$" while the edges are "$\bullet$", and an example of $|A\rangle \otimes |\partial A\rangle \otimes |\overline{A}\rangle$ is shown in Fig. 4. Following the same logic, we write down the overlap function as

$$\Omega_{w,\mu} = \sum_s \exp\left(\sum_{m=\langle i,j \rangle} K_m s_i s_j + \sum_k h_k s_k \right). \quad (24)$$

This is the partition function of the Ising model with nearest neighbor coupling in the presence of the magnetic field. The classical Ising spin is defined on the $\circ$ sublattice, which forms a square lattice. The parameters K_m and h_k are given by Eq. 23.

An interesting scenario is when taking the measurement on the vertex direction to be X and forcing the

measurement outcome to be $\mu_i = +$, which means that for vertex sites $w_i = 1$ and thus $h_i = 0$. The wave function with forced X measurements on the vertices takes the form

$$|\Psi\rangle^+ = \left(\sum_{\mu_\bullet} \Omega_{w,\mu,h=0} |\mu, w\rangle_\bullet \right) \otimes |+\rangle_\circ \quad (25)$$

where $\{|\mu, w\rangle_\bullet\}$ is the edge measurement basis, and $|+\rangle_\circ \equiv \bigotimes_{i \in \circ} |+\rangle_i$ is the tensor product of $+$ eigenstates of Pauli X on the vertices. As $\Omega_{w,\mu,h=0}$ is the same as the overlap function of the toric code shown in Eq. 12, we thus have

$$|\Psi\rangle^+ = |\Psi\rangle_H^{TC} \otimes |+\rangle_\circ \quad (26)$$

with

$$|\Psi\rangle_H^{TC} = \frac{1}{|\mathcal{C}|} \sum_{l \in \mathcal{C}} |l\rangle_H \text{ with } |l\rangle = \bigotimes_{i \in l, j \notin l} |+\rangle_i \otimes |-\rangle_j \quad (27)$$

where $X_i |\pm\rangle_i = \pm |\pm\rangle_i$. One subtlety here is that the quantum state obtained via vertex X measurement is differed form the toric code state shown in Eq. 9 by Hardmard rotations on each unmeasured sits.
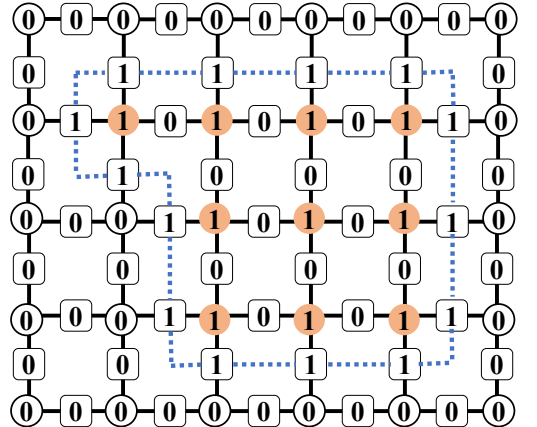

FIG. 4. Example structure of wave function $|A\rangle \otimes |\partial A\rangle \otimes |\overline{A}\rangle$. The Blue dashed loop labels the domain boundary $|\partial A\rangle$, orange dots label $|A\rangle$ and the remaining unlabeled part is $|\overline{A}\rangle$.

Another example is the cluster state defined square lattice state in our previous work [11]. With the bipartition shown in Fig. 3b, the overlap function for this case is

$$\Omega_{w,\mu} = \sum_s \exp\left(\sum_{i \in \bullet} K_i s_a s_b s_c s_d + \sum_{r \in \circ} h_r s_r \right) \quad (28)$$

where the Ising spins $\{s\}$ locate on $\circ$ sites. The four-body Ising interaction $K_i s_a s_b s_c s_d$ is defined on four neighboring sites $a, b, c, d \in \circ$ enclosing site $i \in \bullet$. The effective Ising coupling $\{K_i\}$ and magnetic field $\{h_r\}$ are determined by Eq. 23.

In summary, we show that the overlap function for the ground state of the toric code model and cluster state defined on the bipartite graph can be expressed in terms of classical Ising partition function $\Omega_{w,\mu} = \mathcal{Z}(K,h)$, as shown in Eq. 12, Eq. 21, and Eq. 28. The complexity of simulating the quantum sampling over such resouce states are therefore equivalent to the computational complexity of the corresponding Ising partition function with complex parameters. In the subsequent sections of this paper, we will establish the connection between the complexity of computing this partition function and the entanglement scaling of the 1d boundary state. We will show that by varying the measurement direction $\{w\}$, the boundary state can undergo a volume-law to an area-law entanglement phase transition. This transition, in turn, suggests that the resource state sampling problem can transition from being hard-to-simulate to becoming easy-to-simulate, depending on the measurement direction.

III. BOUNDARY STATES AND ISING PARTITION FUNCTIONS

In this section, we explore the boundary state that arises from measuring the bulk qubits in the previously discussed 2d quantum states. Specifically, we examine the 2d quantum state supported on a half-cylinder denoted as $\mathcal{M}$, as illustrated in Fig. 5. By using Eq.(6), we have

$$|\Psi\rangle_{\partial\mathcal{M}} \propto \sum_{\mu_{\partial\mathcal{M}}} \sum_s \exp\{(H[s])\} |\mu_{\partial\mathcal{M}}, w_{\partial\mathcal{M}}\rangle, \quad (29)$$

where the summation $\sum_{\mu_{\partial\mathcal{M}}} \sum_s$ is over all the spin configurations and boundary basis, and

$$\sum_s \exp\{(H[s])\} \propto \langle \mu_{\mathcal{M}}, w_{\mathcal{M}}, \mu_{\partial\mathcal{M}}, w_{\partial\mathcal{M}} |\Psi\rangle \quad (30)$$

where $|\mu_{\mathcal{M}}, w_{\mathcal{M}}, \mu_{\partial\mathcal{M}}, w_{\partial M}\rangle \equiv |\mu_{\mathcal{M}}, w_{\mathcal{M}}\rangle \otimes |\mu_{\partial\mathcal{M}}, w_{\partial M}\rangle$ is the tensor product of the bulk measurement basis $\{|\mu_{\mathcal{M}}, w_{\mathcal{M}}\rangle\}$ and the boundary basis $\{|\mu_{\partial\mathcal{M}}, w_{\partial\mathcal{M}}\rangle\}$. We will further show that by properly choosing the boundary basis $\{|\mu_{\partial\mathcal{M}}, w_{\partial\mathcal{M}}\rangle\}$, the boundary state can be written in a more compact form as

$$|\Psi\rangle_{\partial\mathcal{M}} \propto \sum_s \exp\{(H[s])\} |s_{\partial\mathcal{M}}\rangle, \quad (31)$$

where $\{|s_{\partial\mathcal{M}}\rangle\}$ is a set of complete basis of the boundary labeled by classical boundary spin configuration $\{s_{\partial\mathcal{M}}\}$.

We first consider the toric code model with a smooth boundary as shown in Fig. 6. We now express the boundary state in Pauli-Z basis $|\mu_{\partial\mathcal{M}}\rangle \equiv \bigotimes_{i\in\partial\mathcal{M}} |\mu_i\rangle_i$, with $\mu_{\partial\mathcal{M}} \equiv (\mu_1, \mu_2, \ldots, \mu_L)$, and $Z_i |\mu_i\rangle_i = \mu_i |\mu_i\rangle_i$. The boundary basis is effectively taking $\theta_i \to 0$ in Eq. 3 on the boundary, and the local weight parameter W_i defined in Eq 4 is then

$$W_i = \lim_{\theta \to 0} \begin{cases} \tan(\theta_i/2)\exp(i\varphi_i) & \text{if } \mu = +1 \\ \cot(\theta_i/2)\exp(-i\varphi_i) & \text{if } \mu = -1 \end{cases}. \quad (32)$$
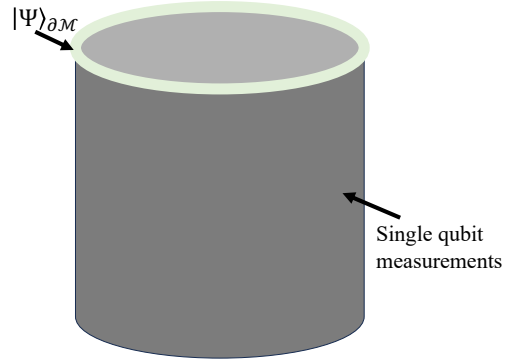

FIG. 5. The quantum state is supported on the half-cylinder $\mathcal{M}$, with single-qubit measurement in the bulk leaving the boundary $\partial\mathcal{M}$ (top circle) qubits unmeasured. $|\Psi\rangle_{\partial\mathcal{M}}$ denotes the wave function of the unmeasured part

For simplicity, we choose the limit direction to be 0^+ to fix the sign of the weight parameter when the measurement outcome is negative $\mu = -1$

$$W_i = \lim_{\theta \to 0^+} \begin{cases} 0 & \text{if } \mu = +1 \\ +\infty & \text{if } \mu = -1 \end{cases} \quad (33)$$

and we thus have the boundary coupling

$$K_i = \begin{cases} +\infty & \text{if } \mu = +1 \\ -\infty & \text{if } \mu = -1 \end{cases}. \quad (34)$$

This can be further written as

$$\tanh K_i = \mu_i \quad i \in \partial\mathcal{M} \quad (35)$$
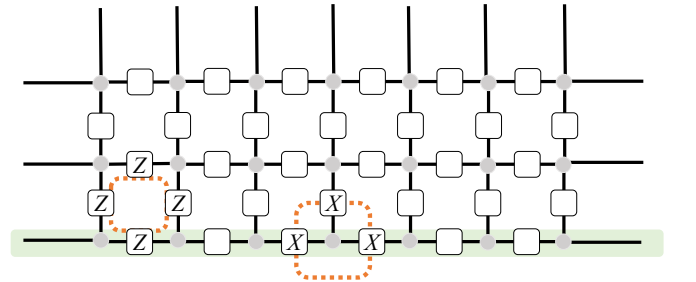
FIG. 6. Toric code with smooth boundary conditions. Green shaded area: boundary qubits. Boundary vertex stabilizer $A_v = \prod_i X_i$ and Plaquette stabilizer $B_p = \prod_i Z_i$ are labeled by orange dashed lines.

The boundary state of the toric code can be expressed as follows:

$$|\Psi\rangle_{\partial\mathcal{M}} \propto \sum_{s,\mu_{\partial\mathcal{M}}} \exp\left(\sum_{j=\langle c,d\rangle} K_j s_c s_d\right) \times \\ \exp\left(\sum_{i=\langle a,b\rangle} K_i s_a s_b\right) |\mu_{\partial\mathcal{M}}\rangle. \quad (36)$$

Here, the first sum, denoted by $\sum_{j=\langle c,d\rangle}$, represents the summation over the links of the bulk of the square lattice, while the second summation $\sum_{i=\langle a,b\rangle}$ is the sum over the links that lie on the boundary. Taking advantage of Eq. 35, we further write the boundary summation as

$$
\exp\left(\sum_{i=\langle a,b\rangle} K_i s_a s_b\right) \propto \prod_{i=\langle a,b\rangle}(1+\tanh K_i s_a s_b)
$$
$$
= \prod_{i=\langle a,b\rangle}(1+\mu_i s_a s_b) \propto \prod_{i\in\partial\mathcal{M}}\delta_{\mu_i,s_a s_b} \tag{37}
$$

where we used the fact that $\prod_{i=\langle a,b\rangle}(1+\mu_i s_a s_b)\neq 0$ if and only if $\mu_i = s_a s_b$ for all i. The boundary state for toric code can now be written as

$$
|\Psi\rangle_{\partial\mathcal{M}} \propto \sum_{\mu_{\partial\mathcal{M}}}\sum_s \exp\left(\sum_{j=\langle c,d\rangle}K_j s_c s_d\right)\prod_{i\in\partial\mathcal{M}}\delta_{\mu_i,s_a s_b}|\mu_{\partial\mathcal{M}}\rangle
$$
$$
\propto \sum_s \exp\left(\sum_{j=\langle c,d\rangle}K_j s_c s_d\right)\bigotimes_{i=\langle a,b\rangle}|s_a s_b\rangle_i. \tag{38}
$$

where $|s_a s_b\rangle_i$ represents the quantum state on the i-th qubit of the boundary, satisfying $Z_i|s_a s_b\rangle_i = s_a s_b|s_a s_b\rangle_i$, with i being the edge connecting neighboring sites a and b. This quantum state is determined by the corresponding classical Ising domain wall configuration on the boundary, denoted as $\{s_a s_b\}$ with a,b being neighbors. With this, we complete the construction of the boundary state for the toric code model.

For the boundary state of the Lieb cluster, similar to the toric code case, we take the basis

$$
|\mu_{\partial\mathcal{M}}\rangle \equiv \left(\bigotimes_{i\in\partial\mathcal{M}_\bullet}|\mu_i\rangle_i\right)\otimes\left(\bigotimes_{a\in\partial\mathcal{M}_\circ}|\mu_a\rangle_a\right). \tag{39}
$$

For the boundary edge qubit $i\in\partial\mathcal{M}_\bullet$, we define the basis as follows

$$
X_i|\mu_i\rangle_i = \mu_i|\mu_i\rangle_i. \tag{40}
$$

For the boundary vertex qubit $a\in\partial\mathcal{M}_\circ$, the basis is

$$
Z_a|\mu_a\rangle_a = \mu_a|\mu_a\rangle_a. \tag{41}
$$

To obtain these basis via the measurement basis defined in Eq. 1, we take $\theta_i\to\pi/2$ and $\phi_i\to 0$ in the Eq. 3. On the other hand, the basis for the vertex qubit $a\in\partial\mathcal{M}_\circ$ is acquired by performing a Pauli Z measurement with $\theta_i\to 0$.

For the edge qubit, the corresponding weight parameter, defined in Eq. 4, of such basis is then

$$
W_i = \begin{cases} 1 & \text{if } \mu_i = +1 \\ -1 & \text{if } \mu_i = -1 \end{cases}. \tag{42}
$$

As $\exp(-2K_i) = (1-W_i)/(1+W_i)$, the corresponding boundary coupling is

$$
K_i = \begin{cases} +\infty & \text{if } \mu_i = +1 \\ -\infty & \text{if } \mu_i = -1 \end{cases}. \tag{43}
$$

Again we write

$$
\tanh K_i = \mu_i \quad i\in\partial\mathcal{M}_\bullet. \tag{44}
$$

As for the boundary vertex qubit, we have

$$
W_a = \begin{cases} 0 & \text{if } \mu_a = +1 \\ +\infty & \text{if } \mu_a = -1 \end{cases}. \tag{45}
$$

The corresponding magnetic field is then

$$
h_a = \begin{cases} +\infty & \text{if } \mu_a = +1 \\ -\infty & \text{if } \mu_a = -1 \end{cases}, \tag{46}
$$

which can be further written as {\color{magenta}VR: How can this equation be correct? $\tanh-\infty = -1$ HL: If $\mu_a = -1$, then $W_a = +\infty$, thus $h_a = -\infty$, and therefore $\tanh h_a = -1 = \mu_a$}

$$
\tanh h_a = \mu_a \quad a\in\partial\mathcal{M}_\circ. \tag{47}
$$

We now write the boundary state of the Lieb cluster state as

$$
|\Psi\rangle_{\partial\mathcal{M}} \propto \sum_{\mu_{\partial\mathcal{M}}}\sum_s \exp\left\{\sum_{j=\langle c,d\rangle}K_j s_c s_d + \sum_e h_e s_e\right\}
$$
$$
\times \exp\left\{\sum_{i=\langle a,b\rangle}K_i s_a s_b + \sum_c h_c s_c\right\}|\mu_{\partial\mathcal{M}}\rangle, \tag{48}
$$

where the first line is the bulk term and the second term is the boundary term. The boundary terms can be futher written as

$$
\exp\left\{\sum_{i=\langle a,b\rangle}K_i s_a s_b + \sum_c h_c s_c\right\}
$$
$$
\propto \prod_{i=\langle a,b\rangle}(1+\tanh K_i s_a s_b)\prod_c(1+\tanh h_c s_c) \tag{49}
$$
$$
\propto \prod_{i=\langle a,b\rangle}\delta_{\mu_i s_a s_b}\prod_c\delta_{\mu_c s_c}.
$$

where we used the same derivation in Eq. 37. We may thus relabel the boundary basis using the boundary Ising spin variables

$$
\begin{aligned}
\mu_i &= s_a s_b & i\in\partial\mathcal{M}_\bullet \\
\mu_c &= s_c & c\in\partial\mathcal{M}_\circ
\end{aligned} \tag{50}
$$

where $i = \langle a,b\rangle$ is the edge connecting neighboring sites a,b. The boundary state of the Lieb lattice model is thus

$$
|\Psi\rangle_{\partial\mathcal{M}} \propto \sum_s \exp\left\{\sum_{j=\langle c,d\rangle}K_j s_c s_d + \sum_e h_e s_e\right\}\times
$$
$$
\bigotimes_{i=\langle a,b\rangle,c}|s_a s_b\rangle_i|s_c\rangle_d. \tag{51}
$$

where the boundary basis satisfies

$$\begin{array}{ll} X_i \ket{s_a s_b}_i = s_a s_b \ket{s_a s_b}_i & i \in \partial\mathcal{M}_\bullet \\ Z_c \ket{s_c}_c = s_c \ket{s_c}_c & c \in \partial\mathcal{M}_\circ \end{array}. \tag{52}$$

It is thus obvious that the boundary state is the eigenstate of $g_i = X_i Z_a Z_b$ with a, b being neighboring boundary sites connected by edge i

$$g_i \ket{\Psi}_{\partial\mathcal{M}} = \ket{\Psi}_{\partial\mathcal{M}} \quad \forall i \in \partial\mathcal{M}_\bullet. \tag{53}$$

The boundary state of the cluster state on the square lattice is obtained using a similar approach as the one defined on the Lieb lattice. The boundary state is

$$\ket{\Psi}_{\partial\mathcal{M}} \propto$$
$$\sum_s \exp\left\{ \sum_{j \in \bullet} K_j s_e s_f s_g s_h + \sum_{r \in \circ} h_r s_r \right\} \tag{54}$$
$$\bigotimes_{i,d} \ket{s_a s_b s_c}_i \ket{s_d}_d$$

where j is the bulk $\bullet$ site enclosed by neighboring $\circ$ sites e, f, g, h, and i labels the boundary $\bullet$ sites enclosed by $a, b, c \in \circ$, as shown in Fig. 7b. The boundary basis satisfies

$$\begin{aligned} X_i \ket{s_a s_b s_c}_i &= s_a s_b s_c \ket{s_a s_b s_c}_i \\ Z_d \ket{s_d}_d &= s_d \ket{s_d}_d \end{aligned} \tag{55}$$

We thus finish the derivation of the boundary state in terms classical Ising model.

To sum up, in this section, we have demonstrated that the boundary state, which is obtained through single qubit projective measurements on the bulk qubits, carries crucial information about the partition function of the 2d classical Ising model. Consequently, if we can successfully compute the 1d boundary state for a large system, we can effectively solve the 2d state sampling problem. One promising method for approximately simulating 1d quantum states is the MPS approach. The complexity of this representation relies on the entanglement scaling of the wave function. If the wave function exhibits volume law scaling of entanglement, storing this quantum state becomes challenging, and consequently, computing the corresponding partition function becomes difficult. However, if the state follows an area law scaling of entanglement, it can be efficiently approximated on a classical computer, making approximately compute the corresponding partition function relatively easy. In the next section, we will elaborate on the formalism to compute the boundary state by mapping it to a 1+1d dynamical problem. This approach will provide further insights into understanding and addressing the complexity of the quantum sampling problem.

IV. BRIDGING 2D SAMPLING PROBLEM AND 1+1D CIRCUIT DYNAMICS

In the previous section, we demonstrated that for a cluster state defined on a bipartite graph, the boundary
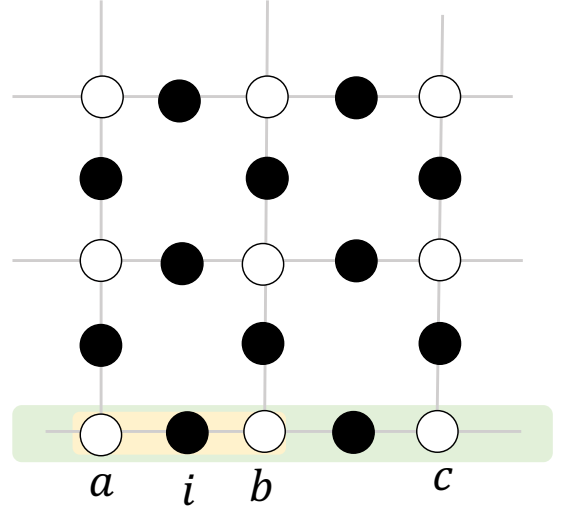
(a) Lieb lattice with smooth boundary. Green shaded area: boundary qubits. $a, b \in \circ$ labels the neighboring sites of $i \in \bullet$. c labels the boundary $\circ$ sites.
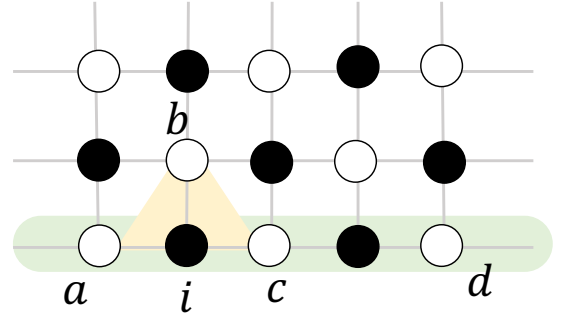
(b) The boundary of the square lattice cluster state. a, b, c labels the neighboring sites of $i \in \bullet$. d labels the boundary $\circ$ sites

FIG. 7. Boundary conventions

1d quantum state can be expressed as follows after performing single qubit measurements on the bulk qubits:

$$\ket{\Psi}_{\partial\mathcal{M}} = \sum_s \exp\{(H[s])\} \ket{s_{\partial\mathcal{M}}} \tag{56}$$

Here $H[s]$ represents a 2d classical spin Hamiltonian with parameters that can take complex values. This boundary state exhibits entanglement transitions and establishes an interesting connection with the 1+1d hybrid quantum dynamics. In this section, we provide three approaches to dynamically generate this boundary state.

A. Transfer matrix method

It is well-established that the partition function of the 2d classical spin model is connected to the 1+1d quantum dynamics using the transfer matrix method. Consequently, the boundary wave function in Eq. (56) can be

expressed as follows:

$$|\Psi\rangle_{\partial\mathcal{M}} = \mathcal{T}\prod_\tau \mathbf{T}(\tau)|\Psi_0\rangle \qquad (57)$$

with $\mathcal{T}$ being time ordering and $|\Psi_0\rangle$ the corresponding initial state with equal weight superposition of all possible boundary classical spin configurations $\{s_{\partial\mathcal{M}}\}$

$$|\Psi_0\rangle \equiv \frac{1}{2^{|\{s_{\partial\mathcal{M}}\}|}}\sum_{s_{\partial\mathcal{M}}}|s_{\partial\mathcal{M}}\rangle. \qquad (58)$$

$\mathbf{T}(\tau)$ is the transfer matrix and corresponds to the quantum evolution operator acting on the 1d quantum state.
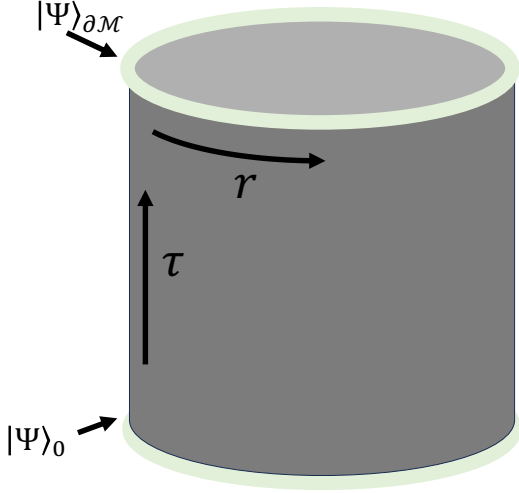

FIG. 8. The two "dimensions" are now labeled as the spacial dimensional r and the temporal dimension τ, $|\Psi\rangle_{\partial\mathcal{M}}$ is obtained by "time" evolution of initial state $|\Psi\rangle_0$

We now use the cluster state defined on the Lieb lattice as an explicit example. Its 1d boundary state is defined in Eq. 51. We take the perpendicular axis as the temporal direction $\hat{\tau}$ and the horizontal axis as the spatial direction $\hat{r}$ shown in Fig. 8. We will use "time slice τ" to refer to the row position of a vertex site. The indices $a, b, c, \ldots$ denote the column position, and $i, j, k, \ldots$ are used to label the edges connecting neighboring vertex sites. We will use $i = \langle a, b\rangle$ to label the edge i connecting neighboring sites a and b, and $e = (k, l)$ to label vertex e shared by neighboring edges k and l.

For the Ising model defined on the square lattice, it is well-known that by associating each vertex with a qubit, we obtain the spin basis for each time slice τ

$$|s\rangle_\tau = \bigotimes_{a\in\tau}|s_a\rangle_a \quad Z_a|s_a\rangle_a = s_a|s_a\rangle_a, \qquad (59)$$

which spans the Hilbert space $\mathcal{H}_\tau = \text{span}\{|s\rangle_\tau\}$. The transfer matrix that maps $\mathcal{H}_\tau$ to $\mathcal{H}_{\tau+1}$ can now be written in the form

$$T(\tau) = T_2(\tau)T_1(\tau) \qquad (60)$$

with

$$T_1(\tau) = \exp\left(\sum_{i=\langle a,b\rangle}K_i^\tau Z_a^\tau Z_b^\tau + \sum_c h_c^\tau Z_c^\tau\right) \qquad (61)$$

$$T_2(\tau) = \exp\left(\sum_e \tilde{K}_e^\tau X_e^\tau\right)$$

with K_i^τ being the quantum Ising coupling, $\tilde{K}_e^\tau$ the effective transverse field, and h_c^τ the longitudinal field. The Paulis are defined in the following way

$$Z_a^\tau \equiv \sum_{s_{a_\tau}}|s_{a_\tau}\rangle_{a_\tau}\langle s_{a_\tau}|_{a_\tau}$$

$$X_e^\tau \equiv \sum_{s_{e_\tau}}|\overline{s_{e_\tau}}\rangle_{e_{\tau+1}}\langle s_{e_\tau}|_{s_{e_\tau}} \qquad (62)$$

where $\overline{s_{e_\tau}} \equiv -s_{e_\tau}$. As $\mathcal{H}_\tau$'s are identical for all time slice τ, we will drop the index τ on the Pauli's as well as on the classical spin indices labeling the quantum states in the remaining part of this section. The relations between the quantum parameters $\{K^\tau, \tilde{K}^\tau, h\}$ and the classical parameters $\{K, h\}$ are shown below

$$K_i^\tau = K_{i_\tau}$$

$$h_c^\tau = h_{c_\tau}$$

$$\tilde{K}_e^\tau = -\frac{1}{2}\ln\tanh K_{e_\tau} \qquad (63)$$

where K_{i_τ} is the classical coupling along the spatial direction $\hat{r}$ on the i-th edge of time slice τ, h_{c_τ} is the classical magnetic field on site c at time slice τ, and K_{e_τ} is the classical coupling along the temporal direction $\hat{\tau}$ of neighboring sites on time slice τ and $\tau+1$ of the e-th row of vertex sites.

In the Lieb lattice model, the qubits are on both the vertices and edges of the square lattice. Notice that the 1d quantum state on the boundary $|\Psi\rangle_{\partial\mathcal{M}}$ is defined on the Pauli-X basis for $\circ$ vertices and the Pauli-Z basis for $\bullet$ edges as shown in the previous section. The basis for the transfer matrix of the Lieb lattice model is naturally

$$|s\rangle_{\text{Lieb}} = \bigotimes_{i,c}|s_a s_b\rangle_i \otimes |s_c\rangle_c \qquad (64)$$

as defined in Eq.52, with $i \in \bullet$ labeling the boundary edge connecting vertex a, b, and $c \in \circ$ the boundary vertex. On such basis, the transverse field part is modified to

$$\mathbf{T}_2(\tau) = \exp\left(\sum_{e=(k,l)}\tilde{K}_e^\tau X_e Z_k Z_l\right), \qquad (65)$$

where again $\tilde{K}_e^\tau = -1/2\ln\tanh K_{e_\tau}$ with K_{e_τ} being the classical coupling along $\hat{\tau}$ that connects neighboring sites of e-th row of vertices on time slice τ and $\tau + 1$. Here, X_e is a Pauli X operator on the vertex qubit e, and Z_k, Z_l are Z Paulis operators on neighboring edges in the

spacial direction $k, l \in \hat{r}$ that share the same vertex e. Since the edge qubits

$$Z_k |s_e s_g\rangle_k = |\overline{s_e s_g}\rangle_k, \tag{66}$$

where $|s_e s_g\rangle_k$ and $|\overline{s_e s_g}\rangle_k$ are the eigenstates of X_k, operator $X_e Z_k Z_l$ flips the classical spin defined on vertex e in the following manner

$$\begin{aligned}
X_e Z_k Z_l |s_e\rangle_e |s_e s_g\rangle_k |s_e s_h\rangle_l \\
= |\overline{s_e}\rangle_e |\overline{s_e s_g}\rangle_k |\overline{s_e s_f}\rangle_l \\
= |\overline{s_e}\rangle_e |\overline{s_e} s_g\rangle_k |\overline{s_e} s_f\rangle_l.
\end{aligned} \tag{67}$$

Here $e = (k, l)$ is the site shared by two edges k and l.

The spatial coupling of the Lieb lattice model $\mathbf{T}_1(\tau)$ is the same as $T_1(\tau)$ for the Ising model defined on a square lattice, since Pauli Z transforms spin-edge basis Eq. 64 the same way as the spin basis Eq. 59. The transfer matrix $\mathbf{T}(\tau) = \mathbf{T}_1(\tau)\mathbf{T}_2(\tau)$ at time τ is thus obtained. The initial state is simply

$$|\Psi\rangle_0 = \frac{1}{2^{|\{s_{\partial\mathcal{M}}\}|}} \sum_{s \in s_{\partial\mathcal{M}}} \bigotimes_{c,i} |s_c\rangle_c \otimes |s_a s_b\rangle_i \tag{68}$$

with a, b, c being vertices, and $i = \langle a, b \rangle$. This state is a 1d cluster state, which means that $g_i = X_i Z_a Z_b$ is a stabilizer of the initial state $|\Psi\rangle_0$. Since

$$[g_i, \mathbf{T}(\tau)] = 0 \quad \forall i, \tau \tag{69}$$

with $i = \langle a, b \rangle$, the boundary state state $|\Psi\rangle_{\partial\mathcal{M}}$ obtained by evolving $|\Psi\rangle_0$ is still an eigenstate of g_i. This is consistent with Eq. 53. We thus finish the derivation of the transfer matrix of the cluster state defined on the Lieb lattice.

B. Connection with 1+1d circuit dynamics

The transfer matrix of the Lieb lattice model obtained in the previous section can be decomposed into three types of local gates in the following way

$$\begin{aligned}
\mathbf{T}(\tau) = &\exp\left(\sum_{i=\langle a,b \rangle} K_i^\tau Z_a Z_b + \sum_c h_c^\tau Z_c \right) \\
&\times \exp\left(\sum_{e=(k,l)} \tilde{K}_e^\tau X_e Z_k Z_l \right) \\
= &\prod_i \mathbf{T}_{ZZ}^{i=\langle a,b \rangle}(\tau) \prod_c \mathbf{T}_Z^c(\tau) \prod_e \mathbf{T}_X^{e=(k,l)}(\tau),
\end{aligned} \tag{70}$$

where

$$\mathbf{T}_{ZZ}^{i=\langle a,b \rangle}(\tau) = \exp(K_i^\tau Z_a Z_b) \tag{71}$$

is a two-qubit gate and characterizes the Ising interaction between neighboring qubits a and b,

$$\mathbf{T}_Z^c(\tau) = \exp(h_c Z_c), \tag{72}$$

is a single qubit gate and represents the longitudinal field acting on vertex qubit c, and

$$\mathbf{T}_X^{e=(k,l)}(\tau) = \exp\left(\tilde{K}_e^\tau X_e Z_k Z_l \right) \tag{73}$$

is a three-qubit gate, where $e = (k, l)$ is the vertex connecting two neighboring edges k and l.

Taking advantage of Eq.23 and Eq.63, the correspondence between parameters in the quantum gates $\{K^\tau, \tilde{K}^\tau, h^\tau\}$ and the weight parameters $\{W\}$ defined in Eq. 4 is then

$$\begin{aligned}
\exp(-2K_i^\tau) &= \frac{1 - W_{i_\tau}}{1 + W_{i_\tau}} \\
\exp\left(-2\tilde{K}_e^\tau\right) &= W_{e_\tau} \\
\exp(-2h_c^\tau) &= W_{c_\tau}
\end{aligned}, \tag{74}$$

where W_{i_τ} and W_{e_τ} are weight parameters on edges in spatial $\hat{r}$ and temporal $\hat{\tau}$ direction respectively. Here i_τ is the i-th edge on time slice τ and e_τ labels the edge connecting neighboring sites on the e-th row of vertex sites on time slice τ and $\tau+1$. W_{c_τ} is the measurement weight parameter on vertex site c of time slice τ. For measurements in the XZ-plane, the weight parameter $W \in \mathbb{R}$. For measurements containing Y components, the weight parameter W becomes complex, and the parameters in both the classical 2d Hamiltonian and 1+1d quantum dynamics are complex.

1. Pauli measurements

To illustrate the correspondence between the 2d measurement process and the $1 + 1$d circuit dynamics and to understand the physical meaning of the complex Ising parameters, we examine three straightforward cases: measuring all the bulk qubits along the X, Z, and Y directions. We show that bulk measurements along X and Z directions can be effectively treated as projective measurements in the $1 + 1$d circuit dynamics, while bulk Y measurements are effective unitary gates.

When measuring the bulk along X direction, we take $W = \pm 1$, where the $\pm$ sign is determined by measurement outcome. For every site in bulk, we have

$$\begin{aligned}
K_i^\tau &= \pm\infty \\
\tilde{K}_e^\tau &= 0 \text{ or } \pm\frac{i\pi}{2}. \\
h_c^\tau &= 0 \text{ or } \pm\frac{i\pi}{2}
\end{aligned} \tag{75}$$

The local terms are

$$\begin{aligned}
\mathbf{T}_{ZZ}^{i=\langle a,b \rangle}(\tau) &\propto (1 \pm Z_a Z_b) \\
\mathbf{T}_Z^c(\tau) &\propto I \text{ or } Z_c \\
\mathbf{T}_X^{e=(k,l)}(\tau) &\propto I \text{ or } X_e Z_k Z_l
\end{aligned}. \tag{76}$$

In this case, $\mathbf{T}_{ZZ}^{i=\langle a,b\rangle}(\tau)$ is effectively a Z_aZ_b projective measurement on neighboring sites a and b connected by edge i, and $\mathbf{T}_Z^c(\tau)$ and $\mathbf{T}_X^{e=(k,l)}(\tau)$ are local unitary Pauli operations that do not affect the entanglement structure. The boundary state $|\Psi\rangle_{\partial\mathcal{M}}$ in this case is stabilized under

$$\mathcal{G} = \langle \pm X_i, \pm Z_a Z_b \rangle \tag{77}$$

which is a trivial product state. For Pauli Z measurements, we have $W = 0, +\infty$ depending on the measurement outcome μ, and the transfer matrix parameters are

$$\begin{aligned} K_i^\tau &= 0 \text{ or } \pm\frac{i\pi}{2} \\ \tilde{K}_e^\tau &= \pm\infty \\ h_c^\tau &= \pm\infty. \end{aligned} \tag{78}$$

The local terms of the transfer matrices thus become

$$\begin{aligned} \mathbf{T}_{ZZ}^{i=\langle a,b\rangle}(\tau) &\propto I \text{ or } Z_a Z_b \\ \mathbf{T}_Z^c(\tau) &\propto (1 \pm Z_c) \\ \mathbf{T}_X^{e=(k,l)}(\tau) &\propto (1 \pm X_e Z_k Z_l) \end{aligned} \tag{79}$$

where a and b denote neighboring sites connected by edge i, c labels the vertex sites, and k, l are edges sharing the same vertex e. At the final time, the quantum state is projected onto the 1-dimensional cluster state up to some Paulis. The reason is that the edges connecting the boundary and bulk are in the temporal direction due to the boundary condition we take, meaning that at the final time the transfer matrix is the temporal part

$$\prod_e \mathbf{T}_X^{e=(k,l)} \propto \prod_{e=(k,l)} (1 \pm X_e Z_k Z_l), \tag{80}$$

which projects the quantum state onto the eigenstate of $\{X_e Z_k Z_l\}$

$$X_e Z_k Z_l |\Psi\rangle_{\partial\mathcal{M}} = \mp X_e Z_k Z_l \quad \forall e = (k,l). \tag{81}$$

The initial state $|\Psi\rangle_0$ is the eigenstate of $\{g_i = X_i Z_a Z_b\}$ with $i = \langle a,b\rangle$ being the edge connecting neighboring sites a and b and g_i commute with all the transfer matrices as shown in Eq. 53 and Eq. 69. The boundary state $|\Psi\rangle_{\partial\mathcal{M}}$ obtained by measuring the bulk in the Z direction is therefore a stabilizer state under group

$$\mathcal{G} = \langle X_i Z_a Z_b, \mp X_e Z_k Z_l \rangle \quad i = \langle a,b\rangle, \ e = (k,l) \tag{82}$$

where the sign $\mp$ is determined by the measurement outcomes. Such a quantum state can be recognized as a 1d cluster state up to some Paulis. This result is consistent with direct calculation using the stabilizer measurement formula shown in [1].

When taking Pauli Y measurements in bulk, the transfer matrix parameters are

$$\begin{aligned} K_i^\tau &= \pm\frac{i\pi}{4} \\ \tilde{K}_e^\tau &= \pm\frac{i\pi}{4}, \\ h_c^\tau &= \pm\frac{i\pi}{4} \end{aligned} \tag{83}$$

and the local terms all become $\frac{\pi}{4}$ Pauli rotations

$$\begin{aligned} \mathbf{T}_{ZZ}^{i=\langle a,b\rangle}(\tau) &= \exp\left(\pm i\frac{\pi}{4} Z_a Z_b\right) \\ \mathbf{T}_Z^c(\tau) &= \exp\left(\pm i\frac{\pi}{4} Z_c\right) \\ \mathbf{T}_X^{e=(k,l)}(\tau) &= \exp\left(\pm i\frac{\pi}{4} X_e Z_k Z_l\right) \end{aligned} \tag{84}$$

By randomly measuring the bulk along the X Y and Z, we obtain an effective $1+1$-dimensional hybrid random circuit. In the next section, we will further show that such a system exhibits a volume-law-area-law entanglement transition on the unmeasured boundary.

2. Free fermion dynamics

As the 2-dimensional Ising model is exactly solvable when $h_c = 0$ for all site c, we discuss the corresponding exact solvable limit of the boundary state $|\Psi\rangle_{\partial\mathcal{M}}$ of the Lieb lattice model. As is shown in previous sections, measuring all the vetex qubits in X direction effectively turns off the magnetic field. We now consider the case where all the vertex qubits including those on the boundary are measured in X direction. For the bulk measurements, we have $W_c = \pm 1$ in the bulk, which means that

$$h_c = 0 \text{ or } \frac{i\pi}{2} \tag{85}$$

depending on the measurement result. The negative measurement result induces an $i\pi/2$ magnetic field, which effectively is an single site Z rotation, and that does not change free-femrion nature of the effective quantum dynamics. The transfer matrices are

$$\begin{aligned} \mathbf{T}_{ZZ}^{i=\langle a,b\rangle}(\tau) &= \exp(K_i Z_a Z_b), \\ \mathbf{T}_X^{e=(k,l)}(\tau) &= \exp\left(\tilde{K}_e^\tau X_e Z_k Z_l\right). \end{aligned} \tag{86}$$

As the transfer matrices are written in the spin-edge basis given in Eq. 64, and notice that $Z_a Z_b$ transforms the basis the same way as X_i with $i = \langle a,b\rangle$

$$X_i |s_a s_b\rangle_i |s_a\rangle_a |s_b\rangle_b = Z_a Z_b |s_a s_b\rangle_i |s_a\rangle_a |s_b\rangle_b, \tag{87}$$

which yields the equivalence relation $Z_a Z_b \sim X_i$. The transfer matrix is further written as

$$\begin{aligned} \mathbf{T}_{ZZ}^{i=\langle a,b\rangle}(\tau) &= \exp(K_i X_i), \\ \mathbf{T}_X^{e=(k,l)}(\tau) &= \exp\left(\tilde{K}_e^\tau X_e Z_k Z_l\right). \end{aligned} \tag{88}$$

X-measurement on the boundary vertex qubits is described by projection

$$\mathcal{P}_X^\pm = \frac{1}{2^L} \prod_{e\in\partial\mathcal{M}} (1 \pm X_e) \tag{89}$$

where e labels the boundary vertex sites, and L is the number of boundary vertex sites. Such projection operator introduces an equivalence relation

$$X_e Z_k Z_l \sim Z_k Z_l \quad e = (k, l) \qquad (90)$$

in the following manner

$$\mathcal{P}_X^{\pm} X_e Z_k Z_l = \mp \mathcal{P}_X^{\pm} Z_k Z_l, \quad \forall e = (k, l), \qquad (91)$$

since $(1 \pm X_e) X_e Z_k Z_l = \mp (1 \pm X_e) Z_k Z_l$. The transfer matrices are now modified to

$$\begin{aligned} \mathbf{T}_{ZZ}^{i=\langle a,b \rangle}(\tau) &= \exp(K_i X_i), \\ \mathbf{T}_X^{e=(k,l)}(\tau) &= \exp\left(\tilde{K}_e^\tau Z_k Z_l \right). \end{aligned} \qquad (92)$$

Such matrices can be further written in the bi-linear form of majorana operators γ_i's via Jordan-Wigner Transformation $i\gamma_{2i-1}\gamma_{2i} = X_i$, $i\gamma_{2k}\gamma_{2k+1} = Z_k Z_{k+1}$ with $\{\gamma_i, \gamma_j\} = 2\delta_{i,j}$,

$$\begin{aligned} \mathbf{T}_{ZZ}^{i=\langle a,b \rangle}(\tau) &= \exp\left(iK_i \gamma_{2i-1}\gamma_{2i} \right), \\ \mathbf{T}_X^{e=(k,l)}(\tau) &= \exp\left(i\tilde{K}_e^\tau \gamma_{2k}\gamma_{2k+1} \right), \end{aligned} \qquad (93)$$

where e labels the edge connecting vertex k and $k+1$. As for random pauli measurement on the edge, the transfer matrices are, up to some pauli rotations,

$$\begin{aligned} \mathbf{T}_{ZZ}^{i=\langle a,b \rangle}(\tau) &\propto (1 \pm X_i) \\ \mathbf{T}_X^{e=(k,l)}(\tau) &\propto (1 \pm Z_k Z_l), \end{aligned} \qquad (94)$$

with i, k, and l labeling the edge qubits and k, l being neighboring edges. Here $\mathbf{T}_{ZZ}^{i=\langle a,b \rangle}(\tau)$ is induced by Pauli-X measurement on the spatial edge i at time slice (τ), while $\mathbf{T}_X^{e=(k,l)}$ is induced by Pauli-Z measurement on the temporal edge connecting vertices on time slice τ and $\tau + 1$. Bulk Y measurements are effectively

$$\begin{aligned} \mathbf{T}_{ZZ}^{i=\langle a,b \rangle}(\tau) &= \exp\left(\pm i\frac{\pi}{4} X_i \right) \\ \mathbf{T}_X^{e=(k,l)}(\tau) &= \exp\left(\pm i\frac{\pi}{4} Z_k Z_l \right). \end{aligned} \qquad (95)$$

It is easy to identify them as the braiding gates of the Majoranas in terms of the free fermion representation of the Ising model. Such dynamics is the same as in [3]. As Pauli-X measurement on the vertex qubits of the Lieb lattice model projects the Lieb cluster state $|\Psi\rangle$ to the toric code state $|\Psi\rangle_{TC}$ up to some Paulis, in this limit, we have the same model as a recent work [17], where the boundary entanglement structure of conducting random measurement in the bulk of toric code model is investigated.

C. Dynamics from Tensor Contractions

Another dynamical interpretation of this model is provided by considering its tensor network representation.

While the method pioneered in [6] provides a generic algorithm to sample from 2d shallow circuits – such as the circuits used to prepare cluster states – we instead use a more direct method that utilizes the exact form of the tensors that constitute the cluster state.

Certain 2d states (such as the cluster state) can be represented as a network of tensors [10, 18, 19], with each index of a tensor represented as a "leg", with the understanding that legs that are connected correspond to indices that are summed over. Each tensor further has a physical index, corresponding to the physical degrees of freedom (qubits, in our case). We distinguish these physical legs from the others by terming the latter "virtual" legs. The process of measuring a qubit in the Pauli Z basis is equivalent to fixing a specific value 0 or 1 of its physical index, which effects a projection $|0\rangle\langle 0|$ or $|1\rangle\langle 1|$ on that qubit. Measurements in other bases can be implemented by applying an appropriate single-qubit rotation prior to constraining the value of the physical index. At the end of our protocol, the tensor only has physical legs at the top edge. The boundary state that remains after measuring the bulk qubits is obtained by contracting over all the remaining non-physical indices in the bulk of the network. However, owing to the associativity of tensor multiplication and the commutativity of projectors on different sites, we are free to choose the order in which the tensor network can be contracted to obtain the boundary state. A specific pattern of contractions which can be interpreted as the evolution of a 1d state through a random nonunitary circuit is described in the following paragraph and in Fig. 9. This procedure can be used to obtain the boundary state following any set of measurement outcomes (μ, ω).

Concretely, we begin by considering the lowest row of the cluster state, defined on a square lattice with L_x columns and L_y rows. This can be treated as an MPS $|\psi_{\text{virt}}(\tau = 1)\rangle$ where the L_x virtual legs that connect this row to the next serve as physical legs. The tensors in the next row have virtual legs connected to tensors in rows both below and above them, and can be thought of as the Matrix Product Operator (MPO) decomposition of a nonunitary operator. We term this operator T, reminiscent of the transfer matrix from the previous section. The state $|\psi_{\text{virt}}\rangle$ can now be "evolved" nonunitarily by contracting the legs it shares with T, and this process is iteratively continued over subsequent rows until the boundary state (i.e., the L_y^{th} row) is reached. The vertical direction can be reinterpreted as a discrete effective time direction. After $\tau \le L_y - 1$ such rows have been contracted – equivalently, τ "time steps" – the state is

$$|\psi_{\text{virt}}(\tau)\rangle = \frac{\prod_{\tau' < \tau} T(\tau') |\psi_{\text{virt}}\rangle}{\left\| \prod_{\tau' < \tau} T(\tau') |\psi_{\text{virt}}\rangle \right\|}. \qquad (96)$$

The boundary state $|\psi_{\text{edge}}\rangle$ is obtained by contracting $|\psi_{\text{virt}}\rangle$ with the L_y^{th} row, resulting in an MPS with physical indices, as shown in Fig. 9.
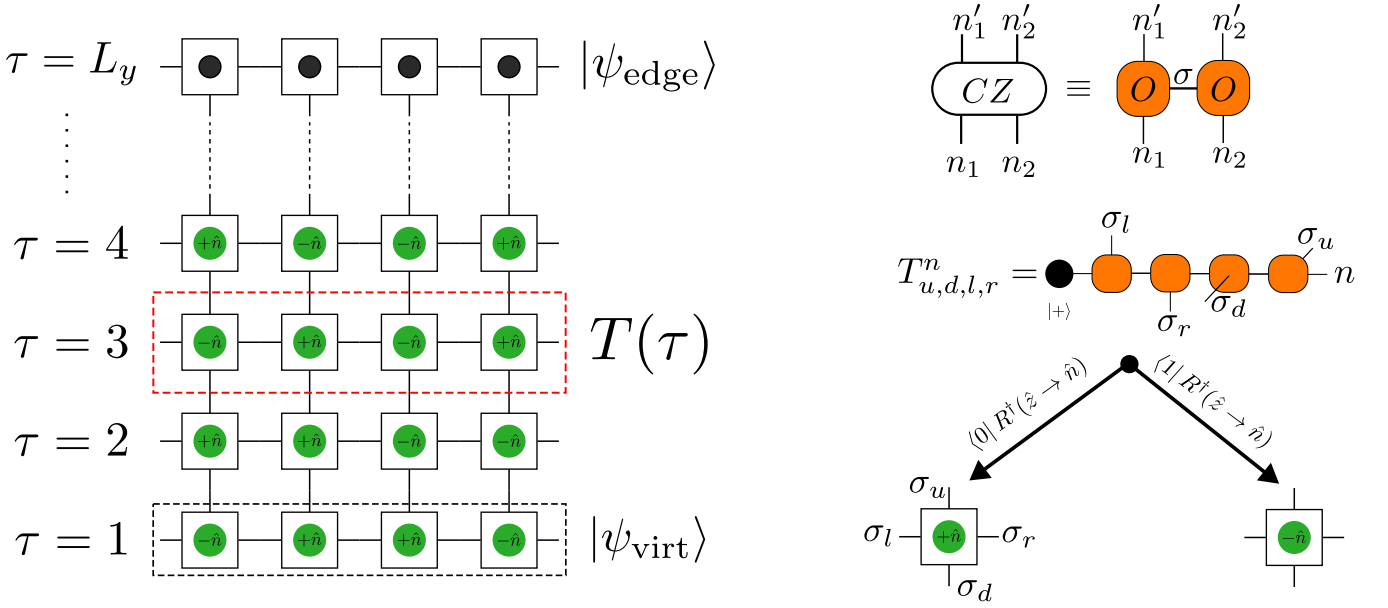
FIG. 9. The process by which $|\psi_{\text{edge}}\rangle$ is obtained on the square lattice. (Left) Each square represents a tensor of the form given in Eq. (106). The green circles denote outcomes (parallel or anti-parallel to the direction $\hat{n}$) for measurements performed on the bulk. The black circles represent the physical degrees of freedom of $|\psi_{\text{edge}}\rangle$. (Right) The decomposition of CZ into MPOs as given in Eq. (100), and the consequent iterative construction of $T^n_{u,l,d,r}$ starting from the $|+\rangle$ state.

1. Obtaining Tensors for the Cluster State

Given a graph G, qubits are initialized in the $|+\rangle$ state – polarized in the X direction – on each vertex of G. For each edge of G, a CZ gate is applied across the vertices that are connected by that edge of G. This results in the cluster state, as defined in Eq. (14). We first derive the tensors for two qubits, labelled 1 and 2, connected by an edge. Initially, $|\psi\rangle_1 = |\psi\rangle_2 = |+\rangle$, and the combined wavefunction can be represented as $|\psi\rangle = \sum_{n_1,n_2=0,1} A^{n_1} A^{n_2} |n_1, n_2\rangle$, where $|n_1, n_2\rangle$ is a state in the computational basis of the 2 qubits. The matrices $A^{n_j} = \frac{1}{\sqrt{2}}$ for $n_j = 0, 1$.

We now turn to the CZ gate, for which we wish to obtain a representation in terms of tensors as

$$CZ = \sum_{\substack{n_1,n'_1 \\ n_2,n'_2,\sigma}} O^{n'_1,n_1}_{\sigma} O^{n'_2,n_2}_{\sigma} |n'_1, n'_2\rangle\langle n_1, n_2|, \quad (97)$$

where $\sum_{n'_j,n_j} O^{n'_j,n_j}_{\sigma} |n'_j\rangle\langle n_j|$ is an operator acting on the jth qubit for each σ. After the application of the CZ gate, the state $|\psi\rangle \to CZ|\psi\rangle = \sum_{n'_1,n'_2,\sigma} B^{n'_1}_\sigma B^{n'_2}_\sigma |n'_1, n'_2\rangle$, where $B^{n'_j}_\sigma = \sum_{n_j} O^{n'_j,n_j}_\sigma A^{n_j}$. The action of the CZ gate is given by

$$CZ |n_1, n_2\rangle = (-1)^{n_1 \cdot n_2} |n_1, n_2\rangle. \quad (98)$$

CZ can equivalently be written as

$$\begin{aligned} CZ &= P^\uparrow_1 + P^\downarrow_1 Z_2 \\ &= 2\left(\frac{1+Z_1}{2}\right)\left(\frac{1+Z_2}{2}\right) - Z_1 Z_2 \\ &= \left(\sqrt{2}P^\uparrow_1 \quad iZ_1\right)\left(\begin{matrix} \sqrt{2}P^\uparrow_2 \\ iZ_2 \end{matrix}\right), \end{aligned} \quad (99)$$

where $P^{0/1}_j \equiv \frac{1\pm Z_j}{2}$ is the projector onto $|0\rangle_j$ or $|1\rangle_j$ and Z_j is the Pauli Z operator, both on the jth qubit. From the last line, $O^{n'_j,n_j}_\sigma$ can be read off as

$$O^{n'_j,n_j}_\sigma = \begin{cases} \sqrt{2}\left(P^0\right)^{n'_j,n_j}, & \sigma = 0 \\ iZ^{n'_j,n_j}, & \sigma = 1 \end{cases}, \quad (100)$$

with $M^{n'_j,n_j} \equiv \langle n'_j|M|n_j\rangle$ for every 1-qubit operator M. Returning to the cluster state, the tensor corresponding to a vertex v, $T^n_{\sigma_1,\sigma_2,\ldots,\sigma_k}$, whose neighbours are $v_1, v_2 \ldots v_k$, and σ_j labels the leg or index shared between v and v_j, is given by

$$T^n_{\sigma_1,\sigma_2,\ldots,\sigma_k} = \frac{1}{\sqrt{2}} \sum_{\{n_j\}=0,1} O^{n,n_1}_{\sigma_1} O^{n_1,n_2}_{\sigma_2} \ldots O^{n_{k-1},n_k}_{\sigma_k}. \quad (101)$$

The (unnormalized) state of T following a measurement is obtained by $\left(P^{\uparrow/\downarrow}\right)^{n,n'} R^{n',n''}(\hat{z} \to \hat{n}) T^{n''}_{\sigma_1,\sigma_2,\ldots,\sigma_k}$, where $R^{n',n''}(\hat{z} \to \hat{n})$ effects a single-qubit rotation from the $\hat{z}$- to the $\hat{n}$-direction, for measurements performed along $\hat{n}$.

As an example, we provide a method by which the tensors for the graph state on the infinite square lattice may be obtained. Let $T^{n_{x,y}}_{u_{x,y},d_{x,y},l_{x,y},r_{x,y}}(x,y)$ denote the tensor corresponding to the qubit located at the vertex (x,y) of the square lattice. n refers to the physical index, while u,d,l and r refer to virtual indices (respectively, the legs that point up, down, left and right). The location dependence of these indices will be suppressed in their notation, unless there is potential for ambiguity. From Eq. (101), with O as in Eq. (100),

$$T^{n}_{u,d,l,r} = \frac{1}{\sqrt{2}} \sum_{\{n_j\}=0,1} O^{n,n_1}_u O^{n_1,n_2}_d O^{n_2,n_3}_l O^{n_3,n_4}_r. \quad (102)$$

This calculation of T only needs to be performed *once*. Following this, the tensors for all other vertices are straightforwardly obtained by relabelling the indices to match the virtual indices of those vertices. By the geometry of the square lattice, the following indices are to be identified:

$$\begin{aligned} r_{x,y} &\leftrightarrow l_{x+1,y} \\ u_{x,y} &\leftrightarrow d_{x,y+1} \end{aligned}. \quad (103)$$

Finally, the graph state can be written as

$$|\psi_G\rangle = \sum_{\{n_{x,y}\}} \sum_{\left\{\substack{u_{x,y},d_{x,y}\\l_{x,y},r_{x,y}}\right\}} \left(\prod_{x,y} T^{n_{x,y}}_{u,d,l,r}(x,y)\delta_{r_{x,y},l_{x+1,y}}\delta_{u_{x,y},d_{x,y+1}} \right) |\{n_{x,y}\}\rangle, \quad (104)$$

with the Kronecker δ symbols enforcing the identification Eq. (103) in the summation. The last step in the MBQC protocol is the measurement of the bulk qubits, leaving behind the edge state $|\psi_{\text{edge}}\rangle$. We choose a uniform direction $\hat{n}$ along which all the bulk measurements are performed. With $\hat{n}$ fixed, the boundary state can uniquely be described by a collection of $L_x \times (L_y - 1)$ bits $\{s_{x,y}\}$, where $s_{x,y} = 0/1$ refers to a measurement resulting in a state parallel ($|+\hat{n}\rangle$) or anti-parallel ($|-\hat{n}\rangle$) to $\hat{n}$ at site (x,y). This step is implemented in two substeps. First, we rotate each qubit using the unitary $\left(R^\dagger(\hat{z} \to \hat{n})\right)^{n_{x,y},n'_{x,y}} |n_{x,y}\rangle\langle n'_{x,y}|$, where $R(\hat{z} \to \hat{n})$ effects a rotation from the $\hat{z}$ axis to $\hat{n}$. Next, we project that bulk qubit on to the state $\langle s_{x,y}|$ by multiplying the tensor $T^{n}_{u,d,l,r}(x,y)$ by an appropriate vector $\left(P^{0,1}\right)^n$ (corresponding to a projection onto $\langle 0/1|$). The (unnormalized) edge state $|\psi_{\text{edge}}\rangle$ is finally given by

$$|\psi_{\text{edge}}\rangle \propto \left(\prod_{(x,y)\in\text{bulk}} (P^{s_{x,y}})^{n_{x,y}} \left(R^\dagger\right)^{n_{x,y},n'_{x,y}} \times \right.$$
$$\left. T^{n'_{x,y}}_{u,d,l,r}(x,y)\delta_{r_{x,y},l_{x+1,y}}\delta_{u_{x,y},d_{x,y+1}} \right) \quad (105)$$
$$\left(\prod_{x,y=L_y} T^{n_{x,y}}_{d,l,r}(x,y)\delta_{r_{x,y},l_{x+1,y}} |n_{x,y}\rangle \right),$$

with the understanding that repeated indices are summed over. The absence of u indices in the last line stem from the fact that the topmost row of the square lattice has no neighbors – and hence no virtual indices – above it.

2. Implementing the 1+1d Circuit

The implementation of the 1+1d circuit that reproduces the boundary state of the square lattice once its bulk degrees of freedom have been measured can now be described in detail. We begin by noting that the expression for $|\psi_{\text{edge}}\rangle$ in Eq. (105) consists of several tensor multiplications, and will focus first on the terms in the first paranthesis. There are two types of multiplications involved in this process – those involving contractions of the physical indices n and those involving the virtual indices $\{u,d,l,r\}$. Crucially, the order in which these contractions are performed is irrelevant to the final solution, since matrix multiplication is associative. No contraction of the physical indices involves more than 1 site at a given time. By choosing the order of contractions, an interpretation of this process as a quantum circuit follows naturally. This can be demonstrated by considering the terms in the parentheses corresponding to the lowest row and subsequent rows separately. We proceed by expressing $\delta_{u_{x,y},d_{x,y+1}}$ as the inner-product of basis states as $\delta_{u_{x,y},d_{x,y+1}} \equiv \langle d_{x,y+1}|u_{x,y}\rangle$, and defining, for $1 < y < L_y$,

$$T_{u,d,l,r}(x,y) \equiv (P^{s_{x,y}})^n \left(R^\dagger\right)^{n,n'} T^{n'}_{u,d,l,r}(x,y), \quad (106)$$

and for $y = 1$ (since these tensors – being those on the last row of the lattice – do not have any virtual indices "below" them, as shown in Fig. 9),

$$B_{u,l,r}(x) \equiv (P^{s_{x,1}})^n \left(R^\dagger\right)^{n,n'} T^{n'}_{u,l,r}(x,1). \quad (107)$$

The term in the first parentheses can be rewritten as

$$\prod_{x,1<y\le L_y-1} T_{u,d,l,r}(x,y)\delta_{r_{x,y},l_{x+1,y}} \langle d_{x,y+1}|u_{x,y}\rangle \times$$
$$\prod_{x,y=1} B_{u,l,r}(x)\delta_{r_{x,1},l_{x+1,1}} \langle d_{x,2}|u_{x,1}\rangle. \quad (108)$$

The order of the bras and kets can be rearranged to give

$$\langle d_{1,L_y} d_{2,L_y} \dots d_{L_x,L_y}|$$

$$\left(\prod_{x, 1 < y \le L_y - 1} T_{u,d,l,r}(x,y) \delta_{r_{x,y},l_{x+1,y}} |u_{x,y}\rangle\langle d_{x,y}| \right)$$

$$\left(\prod_{x,y=1} B_{u,l,r}(x) \delta_{r_{x,1},l_{x+1,1}} |u_{x,y=1}\rangle \right).$$
(109)

For each $1 < y \le L_y - 1$, we can define an effective time-evolution operator $T(\tau)$ as

$$T(\tau) = \sum_{\substack{\{u_{x,\tau},d_{x,\tau} \\ l_{x,\tau},r_{x,\tau}\}}} \prod_x T_{u,d,l,r}(x,\tau) \delta_{r_{x,\tau},l_{x+1,\tau}} |u_{x,\tau}\rangle\langle d_{x,\tau-1}|,$$
(110)

and thus, express the terms in the first parentheses of Eq. (105) as an inner product $\langle d_{1,L_y} d_{2,L_y} \dots d_{L_x,L_y}|\psi_{\text{virt}}(L_y)\rangle$, where

$$|\psi_{\text{virt}}(L_y)\rangle \equiv T(L_y-1)T(L_y-2)\dots T(2)|\psi_{\text{virt}}(\tau=1)\rangle$$

$$|\psi_{\text{virt}}(\tau=1)\rangle \equiv \left(\prod_{x,y=1} B_{u,l,r}(x) \delta_{r_{x,1},l_{x+1,1}} |u_{x,y=1}\rangle \right),$$
(111)

The vertical coordinate y has been relabelled as an effective temporal direction τ. The time evolution of $|\psi_{\text{virt}}\rangle$ can equivalently be seen as an evolution of the $\{B_{u,l,r}(x)\}_\tau$, according to the rule

$$B_{u,\bar{l},\bar{r}}(x,\tau) = T_{u,l,d,r}(x,\tau) B_{u',l',r'}(x,\tau-1)\delta_{d,u'}, \quad (112)$$

where $\bar{l}$ and $\bar{r}$ denote the combined indices (l,l') and (r,r') respectively.

To obtain the edge state $|\psi_{\text{edge}}\rangle$ at the final step of this dynamical evolution, the operator which maps the free virtual indices $\{u_{x,y=L_y-1}\}$ to the physical indices is $\{n_{x,y=L_y}\}$, denoted by $T(\tau=L_y)$, is given by the last line of Eq. (105) as

$$T(\tau=L_y) = \prod_{x,y=L_y} T_{d,l,r}^{n_{x,y}}(x,y) \delta_{r_{x,y},l_{x+1,y}} |n_{x,L_y}\rangle\langle d_{x,L_y}|.$$
(113)

The tensors for $T(\tau = L_y)$ are those that constitute the top-most row of a graph state on a square lattice. Their d indices must be contracted with the u indices of the MPS describing $|\psi_{\text{virt}}(\tau = L_y - 1)\rangle$ to obtain $|\psi_{\text{edge}}\rangle$. Eq. (105) can finally be expressed as

$$|\psi_{\text{edge}}\rangle \propto \prod_{2 \le \tau \le L_y} T(\tau)|\psi_{\text{virt}}(\tau=1)\rangle.$$
(114)

We conclude this section by providing a brief alogrithm that describes this implementation. Note that Eq. (110)

describes the MPO representation of T, while Eq. (111) describes the MPS representation of the state $|\psi_{\text{virt}}\rangle$. This identification allows us to use the extensively studied techniques for the time-evolution of 1d quantum states.

1. Given a measurement direction $\hat{n}$, the measurement outcomes $\{s_{x,y}\}$, and the dimensions of the square lattice L_x and L_y. Assume $L_y \ge L_x$.

2. Obtain the unitary gate R which effects a rotation from $\hat{z} \to \hat{n}$

3. Calculate and store $B_{u,l,r}$ for both measurement outcomes $s = 0, 1$, using Eq. (107).

   - According to $\{s_{x,y=1}\}$, create an MPS for $|\psi_{\text{virt}}\rangle$, where the tensors at site x are $B_{u,l,r}^{(s_{x,y=1})}$.
   - Designate u as a physical index, and relabel the virtual indices l, r uniquely, ensuring, however, that $r_x = l_{x+1}$ (this enforces $\delta_{r_{x,y},l_{x+1,y}}$).

4. Calculate and store $T_{u,d,l,r}$ for either measurement outcome, using Eq. (106). These tensors $T_{u,d,l,r}(x, y > 1)$ constitute the MPO representations of T.

   - Use standard techniques [19, 20] to "time-evolve" (and truncate, if necessary) the MPS $|\psi_{\text{virt}}\rangle$.
   - Normalize the state $|\psi_{\text{virt}}\rangle$.
   - Repeat this process for $\tau = L_y - 1$ time-steps.

5. Evolve the state with $T(\tau = L_y)$ to obtain $|\psi_{\text{edge}}\rangle$.

V. NUMERICAL RESULTS

In this section, we present the numerical calculation of the boundary entanglement with various bulk measurement configurations.

A. Entanglement Scaling at Arbitrary Measurement Directions

Using the tensor network scheme described in Section IV C, we present results for the entanglement of the boundary state after bulk measurements are performed along an arbitrary direction $\hat{n}$, where $\hat{n}$ makes an angle 2θ with the Z axis. The entanglement is quantified using the 2nd Rényi entropy $S_A^{(2)}$, defined as

$$S_A^{(2)} = -\ln \text{tr}\, \rho_A^2,$$
(115)

where $\rho_A = \text{tr}_{\overline{A}} |\psi_{\text{edge}}\rangle\langle\psi_{\text{edge}}|$ is the reduced density matrix describing subsystem A of the boundary state ψ_{edge}, and $\overline{A}$ is the complement of A.
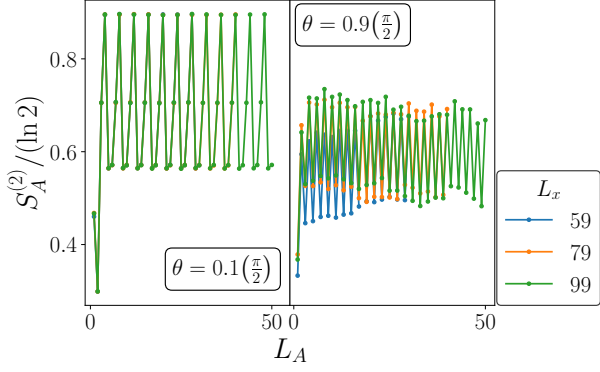
FIG. 10. The entanglement entropy in the boundary state of a Lieb lattice with dimensions $L_y = 500$ and L_x. Measurements are performed along $\hat{n} = \cos(\theta)\hat{z} + \sin(\theta)\hat{x}$. In both cases, S_A shows no dependence on subsystem-size L_A, nor does it change with L_x, indicating an area-law phase.
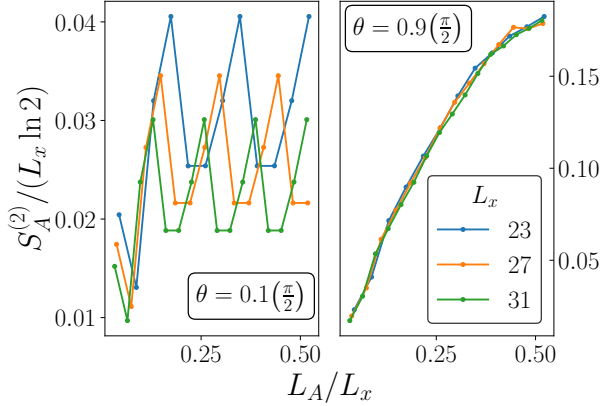

FIG. 11. The scaling of entanglement entropy in the boundary state of a Lieb lattice with dimensions $L_y = 500$ and L_x. Measurements are now performed along $\hat{n} = \cos(\theta)\hat{z} + \sin(\theta)\hat{y}$. (Left) S_A/L_x trends downward as L_x increases, indicating that the entanglement scales sub-linearly. When S_A is plotted as a function of L_A (as in Fig. 10, not shown), the curves superimpose one-another, indicating an area-law phase. (Right) S_A scales linearly with L_x, and the data is amenable to a collapse indicative of a volume law phase.

As initial states, we consider the cluster state defined on (a) the Lieb lattice and (b) the square lattice. For (a), we separately consider the cases where $\hat{n}$ lies in the $X-Z$ plane and the $Y-Z$ plane, while for (b), we only consider the case where $\hat{n}$ lies in the $X-Z$ plane. In what follows, L_x denotes the horizontal width of the state, while L_y denotes the vertical length (or the number of effective time steps). Results are presented for a randomly chosen set of bulk measurement outcomes, and are averaged over ≈ 20 such sets of outcomes to make the data more presentable. We expect these results to capture both the typical and the outcome-averaged behavior of the cluster state. Since the accessible (horizontal) sizes are limited in numerical simulations, we use the following criteria to
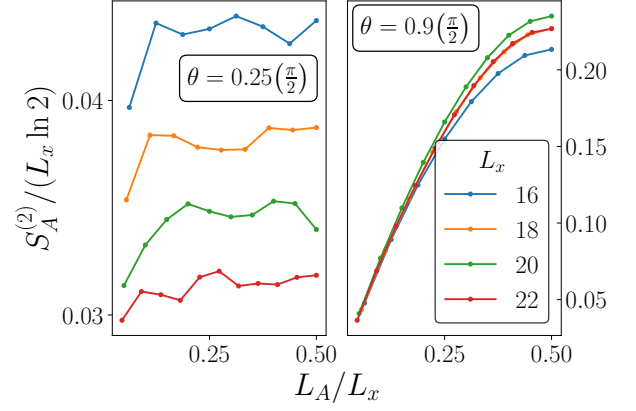

FIG. 12. The scaling of entanglement entropy in the boundary state of a square lattice with dimensions $L_y = 500$ and L_x. Measurements are performed along $\hat{n} = \cos(\theta)\hat{z} + \sin(\theta)\hat{x}$. As in Fig. 11, (Left) S_A/L_x trends downward as L_x increases, while (Right) S_A scales linearly with L_x, indicating a volume law phase.

determine the entanglement scaling behavior: for a given $\hat{n}$, we first plot the scaled entanglement entropy S_A/L_x as a function of fractional subsystem size L_A/L_x for various sizes L_x. If the curves approximately collapse onto a single curve, the boundary state obeys a volume-law scaling ($S_A^{(2)} \sim |A|$). If the curves instead trend downward with increasing L_x, this signals an area-law scaling ($S_A^{(2)} \sim \text{const}$) of the entanglement entropy.

Under certain conditions, we find that the entanglement of the boundary state undergoes a phase transition as the measurement angle θ is varied. This is interesting in its own right, since this transition adds to the panoply of measurement-induced phase transitions. Additionally, such a transition also bears interesting consequences for the feasibility of using an effective 1+1d dynamics to calculate the partition functions of 2D Ising models $\mathcal{Z}$; the entanglement of the boundary state predominantly determines the memory demands of performing such a calculation. In the area-law phase, $\mathcal{Z}$ can be computed efficiently for large system sizes with controlled approximations, but in the volume-law phase, these approximations to $\mathcal{Z}$ are uncontrolled, and thus, the calculations of $\mathcal{Z}$ requires resources exponentially large in L_x. In the 1+1d dynamics, the approximations correspond to retaining only a fixed number of the largest singular values in each of the tensors that constitute $|\psi_{\text{virt}}\rangle$. This can be done with a controlled error only if $|\psi_{\text{virt}}\rangle$ is area-law entangled.

To demonstrate the utility of this connection, we simulate an effective 1+1d evolution that results in a post-measurement state which corresponds to random bond Ising-type models (RBIMs), as in Eq. (51) and **??**. We focus on RBIMs where the absolute values of the interaction parameters ($|K|$) are fixed to be constant across all interacting spins, but their signs ($K/|K|$) take random values ± 1 at each site. This can be achieved by

choosing position-dependent measurement directions and post-selecting for specific measurement outcomes, which are also position-dependent. While conventional wisdom dictates that the presence of negative or complex weights in a partition function generally make the calculation of a partition function $\mathcal{Z}$ difficult, we use this method to show that this is not necessarily the case. Specifically, there are $\mathcal{Z}$ with negative or complex weights that are easy to simulate and those with positive weights that are not. Thus, we posit that the complexity of calculating $\mathcal{Z}$ (using a 1+1d-like algorithm) depends crucially on the form of the interactions in the Hamiltonian of $\mathcal{Z}$ as well.

The simulations for which results are presented were performed using the ITensor Julia package[20, 21].

1. Lieb Lattice - Random Measurement outcomes

In the Lieb lattice, a volume-law entangled phase is absent in the boundary state of a Lieb lattice when $\hat{n}$ lies in the $X - Z$ plane. In this case, one observes two distinct area-law phases separated by a critical, logarithmically entangled phase. The $\mathcal{Z}$ corresponding to this case has negative weights, but we see that this does not lead to a change in the complexity of its calculation. When $\hat{n}$ is instead chosen to lie in the $Y - Z$ plane, an area-law to volume-law transition is observed as θ is tuned through $\theta_c \sim 0.75\left(\frac{\pi}{2}\right)$. $\mathcal{Z}$ now includes complex weights, but it is only above a specific value of θ that this calculation becomes hard. VR: Should I talk about connections to high- and low-T?

2. Square Lattice - Random Measurement outcomes

In contrast to the Lieb Lattice, we find an area- to volume-law transition in the scaling of the entanglement entropy of the boundary state in the square lattice, even as $\hat{n}$ is varied in the $X - Z$ plane. For small θ, the state is area-law entangled, but becomes volume-law entangled as θ exceeds $\theta_c \sim 0.7\frac{\pi}{2}$. Again, here, $\mathcal{Z}$ is entirely of real weights, but the corresponding Ising model now has 4-body interactions Eq. (54), as opposed to 2-body interactions in the Lieb lattice. Using the mapping Eq. (54), we can obtain intuition for the transition. When $\theta = 0$, the Ising interaction strength is either $-\infty$ or 0, depending on the measurement outcome, while the contribution from the magnetic field to the partition function is 0, unless all the outcomes are $-$. In the opposite limit $\theta = \frac{\pi}{2}$, the Ising interactions are equally likely to be ± 1. The increasing relevance of the frustrations arising from the 4-body interactions as θ is varied could be responsible for the poor performance of the 1+1d algorithm.

3. RBIMs on the Lieb- and Square-lattice

We have, thus far, discussed the entanglement scaling as the measurement direction is kept uniform across the lattice, while outcomes are random, as would be the case in an experimental set-up. We have also demonstrated that the resulting boundary state $|\psi_{\text{edge}}\rangle$ can be described in terms of a classical parition function $\mathcal{Z}$. In this subsection, we instead use one class of post-selected trajectories (i.e. measurement outcomes) to glean information about the computational complexity of the corresponding $\mathcal{Z}$ that describes the $|\psi_{\text{edge}}\rangle$. We focus on the specific cases of $\mathcal{Z}$ that describe RBIMs, where the randomness is only in the sign of the Ising interaction. The implementation is described below.

We begin by considering the case where the measurement outcomes are all $+1$, meaning that the measurement outcomes all point along $\hat{n}(x, y)$, but $\hat{n}$ can now be position-dependent. We also choose $\hat{n}$ to lie in the X-Z plane (so $\phi = 0$). From Eq. (23), we see now that the K and h parameters are given by

$$
\begin{aligned}
\exp(-2h_k) &= \tan\left(\theta_k/2\right) & k &\in \circ \\
\exp(-2K_i) &= \frac{1 - \tan\left(\theta_i/2\right)}{1 + \tan\left(\theta_i/2\right)} & i &\in \bullet
\end{aligned}
\tag{116}
$$

Given a value of the magnetic field h_k at site k, we can instead set that term to be $-h_k$ by setting $\theta \to \pi - \theta \implies \tan\left(\theta_k/2\right) \to \tan\left(\pi/2 - \theta_k/2\right) = \cot\left(\theta_k/2\right) = 1/\tan\left(\theta_k/2\right) = \exp(2h_k)$. This, in turn, ensures that the $\mathcal{Z}$ that describes $|\psi_{\text{edge}}\rangle$ has the magnetic field at site k flipped.

Similarly, to toggle only the sign of the interaction K_i from $+ \to -$, only the change $\tan\left(\theta_i/2\right) \to \tan\left(-\theta_i/2\right) \implies \theta_i \to -\theta_i$ needs to be effected. We then consider an evolution where the measurement outcomes are all chosen to be $+1$, but the angle is chosen randomly from $\{\theta, -\theta\}$ for all sites on the $\circ$ sublattice. This models interactions of the form

$$
|K| \sum_{\langle i, j \rangle} \text{sign}(K_{ij}) s_i s_j
\tag{117}
$$

for the Lieb lattice, and

$$
|K| \sum_{\square} \text{sign}(K_i) \prod_{a \in \square} s_a
\tag{118}
$$

for the square lattice; $\square$ denotes plaquettes of the square lattice, and $\text{sign}(K) = \pm 1$ if $\hat{n} = (\cos\theta)\hat{z} \pm (\sin\theta)\hat{x}$.

In the Lieb lattice, we find that the state is *always* in an area-law, which suggests that the partition function of an RBIM with 2-body interactions should always be easily calculable, independent of θ (or $|K|$). In the square lattice, however, we find a transition from an area- to a volume-law, signaling a computational complexity phase transition in the calculation of $\mathcal{Z}$. It remains to be seen what the consequences of this difficulty (if any) are on the phases that a classical Ising model with 4-body interactions can exhibit.

4. Role of Randomness

It must be emphasized that the randomness in the measurement outcomes is crucial to observing any non-area-law phase. If the measurement outcomes are all chosen to be equal (+1, for instance), the boundary state is area-law entangled in the thermodynamic limit $L_y \to \infty$. The finite-size scaling of entanglement is shown in the presence and absence of randomness in (...), in the Lieb lattice, making evident the significance of this stochasticity. This is seen to be the case regardless of the geometry or of $\hat{n}$ (except at a few isolated points). This emphasizes the importance of frustration in making the calculation of $\mathcal{Z}$ hard, which cannot exist if all measurement outcomes and directions – consequently, the Ising interaction strengths – are the same.

B. Entanglement Scaling with Random Pauli Measurements

We begin by investigating the boundary entanglement structure induced by bulk Pauli measurements on a 2D graph state. We first review the dynamical stabilizer method introduced in our previous work [11], and we apply such a method to the Lieb lattice model and investigate the boundary entanglement structure of the Lieb lattice model with random Pauli measurement in the bulk.

For a graph state defined on the specific lattice embedded in a half cylinder shown in Fig. 5. We abstract the model in the following sense. The lattice is now described by identical layers $\{L_\tau, \tau = 1, 2, 3, \ldots\}$ given by the lattice translational symmetry together with entangling controlled-Z gates $\{\mathbf{CZ}_{i,i+1}, i = 1, 2, 3, \ldots\}$ connecting neighboring layers i and $i+1$. As projective measurements on a graph state only affect the neighboring entanglement structure, measuring all the qubits on one layer L_τ will only affect the entanglement structure in L_τ, $L_{\tau-1}$, and $L_{\tau+1}$. Inspired by this fact, the 2 dimensional measurement process can be simulated in a dynamical manner as follows. We first prepare a three-layer graph state, perform pauli measurement in the midlle layer, and discard the measured qubits. Next, we use entangling controlled-Z gates to entangle the remaining two-layer state with a third layer. Iterating this measurement-discard process and at final time measure all the qubits that do not belong to the boundary $\partial \mathcal{M}$, we thus have a dynamical way of constructing the boundary state $|\Psi\rangle_\mathcal{M}$.

For the graph state on the Lieb lattice, we take the single layer of the form shown in Fig. 13. Applying the dynamical evaluation process we obtain the boundary state of the Lieb lattice model. The numerical data is shown in the following part of this section.
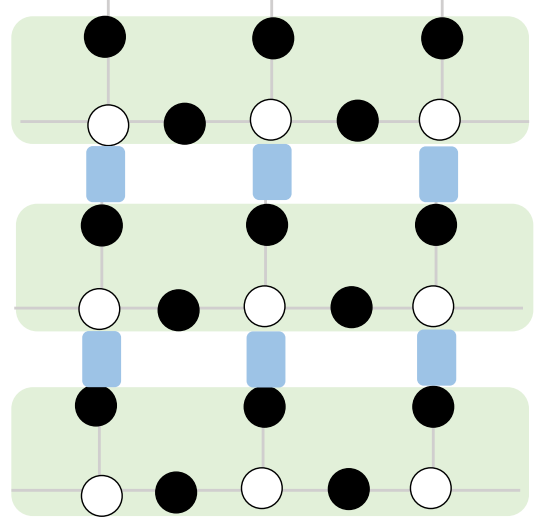

FIG. 13. Lieb lattice layer convention. Green shaded area labels a layer state $|\phi\rangle_{L_\tau}$ and blue blocks are CZ gates entangling neighboring layers.

1. Volume-law-area-law Transition

We consider the graph state defined on the Lieb lattice and perform randomized Pauli X, Y, and Z measurements on the bulk qubits with probabilities p_x, p_y, and p_z, respectively, restricted by

$$p_x + p_y + p_z = 1. \tag{119}$$

We first investigate the scaling of the entanglement entropy

$$S_A = - \operatorname{tr} \rho_A \ln \rho_A \tag{120}$$

on the boundary. Here $\rho_A = \operatorname{tr}_{\overline{A}} \rho$ is the partial trace of the density matrix of the boundary state $\rho = |\Psi\rangle_{\partial \mathcal{M}} \langle \Psi|_{\partial \mathcal{M}}$. In the absence of the Y measurement, the boundary 1d state consistently is area-law entangled $S_A \sim \text{const.}$. However, as shown in Fig. 14, when the Y measurement dominates, the entanglement entropy satisfies volume-law scaling, $S_A \sim |A|$. By adjusting the measurement rate p_y, we induce an entanglement transition from the volume-law phase to the area-law phase. This transition can be mapped to MIPT by the transfer matrix formalism presented in Sec. IV A, where we demonstrated that X or Z measurements correspond to one or two-qubit projective measurements, while the Y measurement corresponds to a two-qubit unitary gate. The interplay between the entangling Y measurement and the disentangling X/Z measurement drives the entanglement phase transition. In the following part of this section, we take L to be the number of qubits on the boundary $\partial \mathcal{M}$, and L_A to be the number of qubits in subsystem A.

The position of the volume-law to area-law entanglement phase transition can be located by the peak of the mutual information
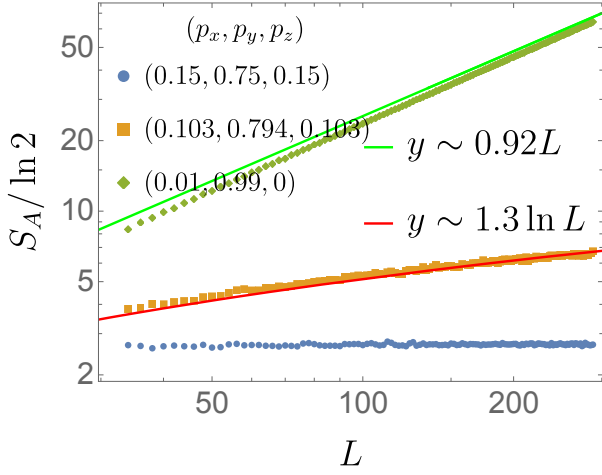
$$I_{AB} = S_A + S_B - S_{AB} \tag{121}$$

FIG. 14. Entanglement entropy S_A scaling of fixed subsystem size $L_A = L/2$

of two antipodal regions A and B on the boundary $\partial \mathcal{M}$ with $L_A = L_B = L/8$ as shown in Fig. 16[1]. Such peak marks the phase boundary and we thus have the phase diagram Fig. 15.
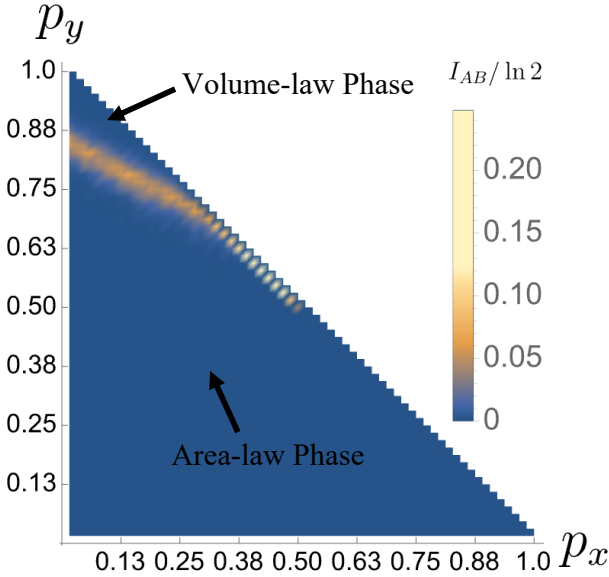

FIG. 15. Mutual information I_{AB} of diagonal domain A and B, with $L_A = L_B = L/8$. The yellow line (mutual information peak) marks the phase boundary.

.

We further explore the entanglement phase transition of the two specific cases: (1) when $p_z = 0$, allowing only X and Y measurements, and (2) when $p_x = 0$, with only random Z and Y measurements.

For $p_z = 0$, where only X and Y Pauli measurements exist, the criticality is observed at $p_y = 0.58$ and $p_x = 0.42$. The mutual information of two antipodal regions

peaks at critical point and collapses to

$$I_{AB} \sim f\big(L^{1/\nu}(p_y - p_y^c)\big)$$
$$p_y^c = 0.58, \quad \nu = 1.78. \tag{122}$$

as shown in Fig. 16b. At criticality, the entanglement entropy scales logarithmically with subsystem size L_A

$$S_A/\ln 2 \sim 0.58 \ln(\sin \pi L_A/L) \tag{123}$$

which is shown in Fig. 17b. At criticality, the mutual information I_{AB} of two disjoint regions A and B is a function of the cross-ratio χ_{AB}. In particular, when χ_{AB} is close to zero, we have
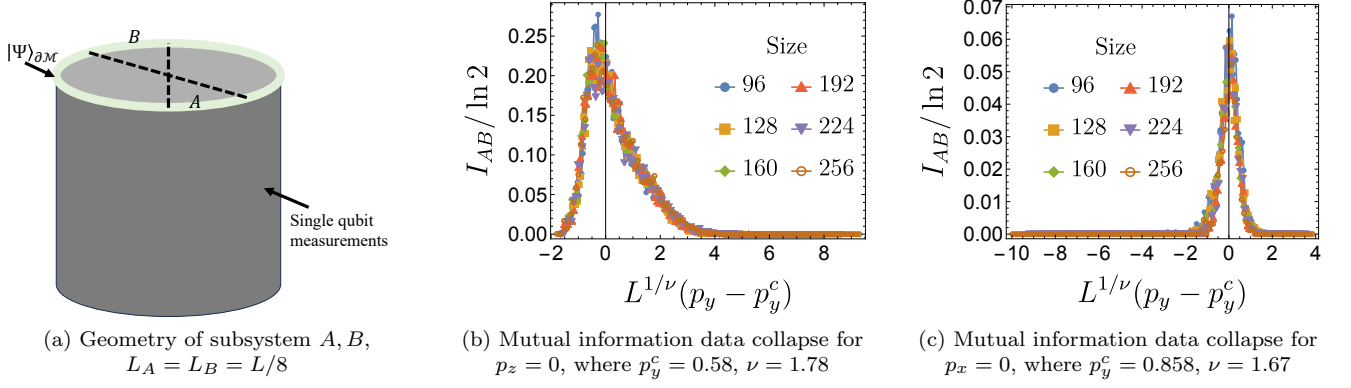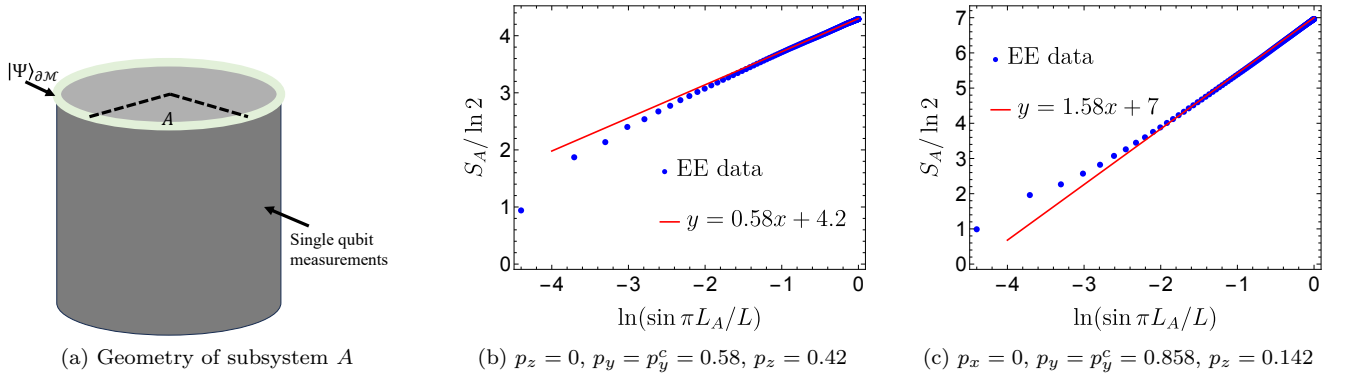
$$I_{AB} \sim \chi_{AB}^{0.6}, \tag{124}$$

where

$$\chi_{AB} = \frac{x_{12}x_{34}}{x_{13}x_{24}}, \quad \text{with } x_{ij} = \frac{L_x}{\pi} \sin\left(\frac{\pi}{L_x}|x_i - x_j|\right), \tag{125}$$

where $x_{i=1,2,3,4}$ are endpoints of subregions A and B as shown in Fig. 18a.

Taking $p_x = 0$, the critical point occurs at $p_y = 0.858$ and $p_z = 0.142$. Fig.17c showing that $S_A/\ln 2 \sim 1.58 \ln(\sin(\pi L_A/L))$. The mutual information I_{AB} data collapse around the critical point is shown in Fig. 16c, where we have $\nu = 1.78$. Furthermore, at criticality, Fig. 19 presents the scaling of mutual information between disjoint intervals A and B, characterized by $I_{AB} \sim \chi_{AB}^2$.

2. Area-law-to-area-law transition

As demonstrated in Eq.26, measuring all the vertex qubits along the X-direction on the Lieb lattice allows us to generate the toric code state up to some Pauli rotation. We further perform randomized Pauli X, Y, and Z measurements in the bulk edge qubits of the Lieb lattice graph state with probabilities p_x, p_y, and p_z, respectively. Using the transfer matrix method detailed in Sec. IV B 2, we can show that this dynamics is equivalent to a free fermion system subject to repeated projective measurements as reported in [3]. The Y measurement generates a unitary free fermion gate, effectively braiding a pair of Majorana fermions, while the X and Z measurements correspond to X and ZZ measurements in the effective $1+1$d dynamics respectively. This non-unitary free fermion dynamics can be mapped to a loop model, which has been extensively studied in Ref. 22. In cases dominated by Y measurements, a critical phase emerges. Increasing p_x or p_z can induce transitions to two area-law phases, notably, in the limit where $p_y = 0$, varying p_x results in an area-law to area-law transition, with the critical point described by the 2d percolation conformal field theory. These different phases can be characterized by their difference in the mutual information I_{AB}. Notably, we consider $L_A = L_B = L/4$ and the

(a) Geometry of subsystem A, B, $L_A = L_B = L/8$

(b) Mutual information data collapse for $p_z = 0$, where $p_y^c = 0.58$, $\nu = 1.78$

(c) Mutual information data collapse for $p_x = 0$, where $p_y^c = 0.858$, $\nu = 1.67$

FIG. 16. Mutual Information data collapse $I_{AB} = f(L^{1/\nu}(p_y - p_y^c))$ for Lieb lattice model

(a) Geometry of subsystem A

(b) $p_z = 0$, $p_y = p_y^c = 0.58$, $p_z = 0.42$

(c) $p_x = 0$, $p_y = p_y^c = 0.858$, $p_z = 0.142$

FIG. 17. Critical entanglement entropy scaling of Lieb lattice model, $S_A \sim \alpha \ln(\sin \pi L_A/L)$

domain distance $r_{AB} = L/2$. The phase diagram is presented in Fig. 21. Our investigation reveals the presence of three discernible phases. In the trivial phase, we have $I_{AB} = 0$. Conversely, in the topological phase, characterized by $I_{AB} = \ln 2$, the system displays long-range entanglement arising from the logical operator $O_L = \prod_{i \in l_n} X_i$ of the toric code induced by the bulk X measurement, where l_n denotes the non-contractable loop of the cylinder. When the Z measurement dominates, the logical operator is pushed onto the boundary contributes the $\ln 2$ of the mutual information between boundary region A and B.

In this model, even with the existence of the effective unitaries induced by the bulk Y measurement, there is no volume-law phase observed. The absence of the volume-law phase agrees with our previous statement that the computation of the Ising model defined in Eq.(24) with $h = 0$ only requires polynomial resource and can be efficiently evaluated on the classical computer. Below, we provide numerical confirmation of these results.

We begin by considering the case where $p_y = 0$ and varying p_x. At criticality, as illustrated in Fig. 19a, the entanglement entropy scales as:

$$S_A / \ln 2 = \frac{K}{2} \ln \left(\sin \left(\frac{\pi L_A}{L} \right) \right), \quad (126)$$

where $K = 0.54 \approx \sqrt{3}/\pi$, which agrees with the theoretical prediction [22]. The critical scaling of the mutual information is given by:

$$I_{AB} \sim \chi_{AB}^{\Delta}, \quad \Delta = 0.33 \sim \frac{1}{3}, \quad (127)$$

as shown in Fig. 19b. Furthermore, we examine the data collapse of the mutual information for two diagonal intervals, A and B, with $L_A = L_B = L/4$. The mutual information collapses to

$$I_{AB} \sim g(L^{1/\nu}(p_x - p_x^c)) \quad (128)$$

with $\nu = 3/4$ and $p_x^c = 0.5$, which can be identified as a bond percolation on a square lattice, which agrees with the result shown in Ref. 3.

Introducing Y measurement can lead to a critical phase where the entanglement entropy scales logarithmically to the leading order

$$S_A / \ln 2 \sim \alpha \ln \left(\sin \left(\frac{\pi L_A}{L} \right) \right) + \mathcal{O} \left(\sin^2(\pi L_A/L) \right), \quad (129)$$

with a being some non-universal constant varies with measurement rate p_x, p_y, p_z. Some entanglement entropy scaling data with $p_x = p_z = (1 - p_y)$ is shown in Fig. 20.
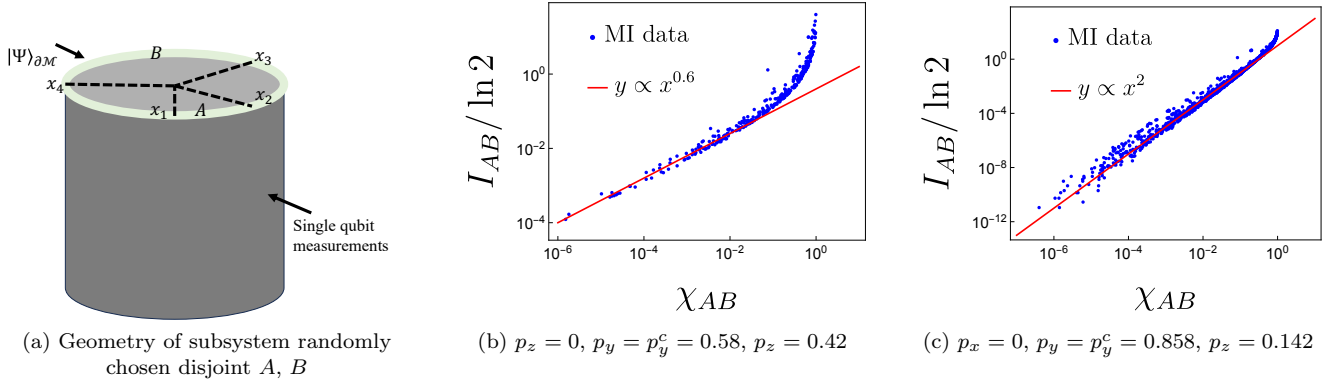
(a) Geometry of subsystem randomly chosen disjoint A, B

(b) $p_z = 0$, $p_y = p_y^c = 0.58$, $p_z = 0.42$

(c) $p_x = 0$, $p_y = p_y^c = 0.858$, $p_z = 0.142$

FIG. 18. Critical mutual information (MI) scaling of Lieb lattice model, $I_{AB} \sim \chi_{AB}^\Delta$

(a) Critical entanglement scaling, $p_x = p_z = 0.5$, $p_y = 0$

(b) Critical mutual information scaling, $p_x = p_z = 0.5$, $p_y = 0$

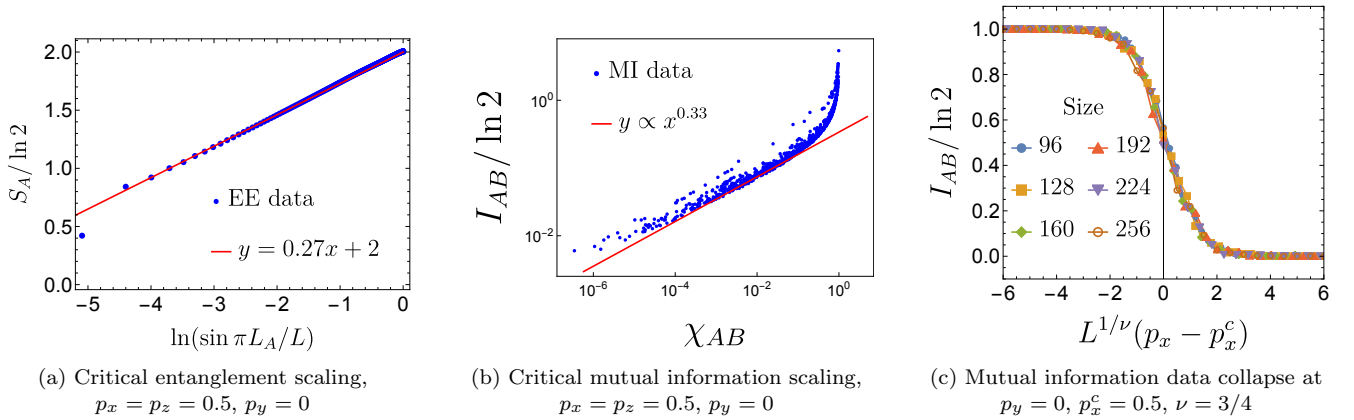(c) Mutual information data collapse at $p_y = 0$, $p_x^c = 0.5$, $\nu = 3/4$

FIG. 19. Criticality of area-law-area-law phase transition at $p_y = 0$, $p_z = p_x = 0.5$

In summary, our numerical observations clearly demonstrate that the 1d boundary state of the Lieb graph state can exhibit a phase transition from a volume-law phase to an area-law phase under bulk random measurements. Notably, this transition is intricately linked to the computational complexity of the 2d Ising partition function in Eq.(24). When the Y measurement rate is large, the unitary gate dominates the corresponding effective 1+1d hybrid circuit dynamics. Consequently, the boundary state exhibits volume-law entanglement, rendering the associated 2d Ising model challenging to compute. Conversely, by constraining the measurement type on the vertex qubits to Pauli X measurements and applying randomized $X/Y/Z$ measurements along the edges, the resulting boundary state becomes mostly limited to logarithmic entanglement. This constraint effectively removes the magnetic field in the 2d Ising model in Eq.(24), and allows for the efficient polynomial-time simulation of the Ising partition function.

VI. DISCUSSION

In this study, we have delved into the different types of boundary entanglement phase transitions induced by measuring various two-dimensional resource states, drawing intriguing connections to transitions in computational complexity and boundary entanglement scaling.

The cornerstone of our investigation lies in the novel connection established between the sampling problem inherent in the two-dimensional graph states on a bipartite lattice and the Ising partition function characterized by complex parameters. This profound correspondence enriches our understanding of the underlying mechanisms governing boundary entanglement phase transitions. It provides a bridge between the abstract realm of quantum information and the well-established framework of statistical mechanics.

Central to our findings is the revelation that the one-dimensional boundary state encapsulates the bulk information in the two-dimensional Ising partition function. The transfer matrix approach of the Ising model emerges as a powerful tool in illuminating the connection between the 2d bulk measurement process and the 1+1d circuit dynamics.
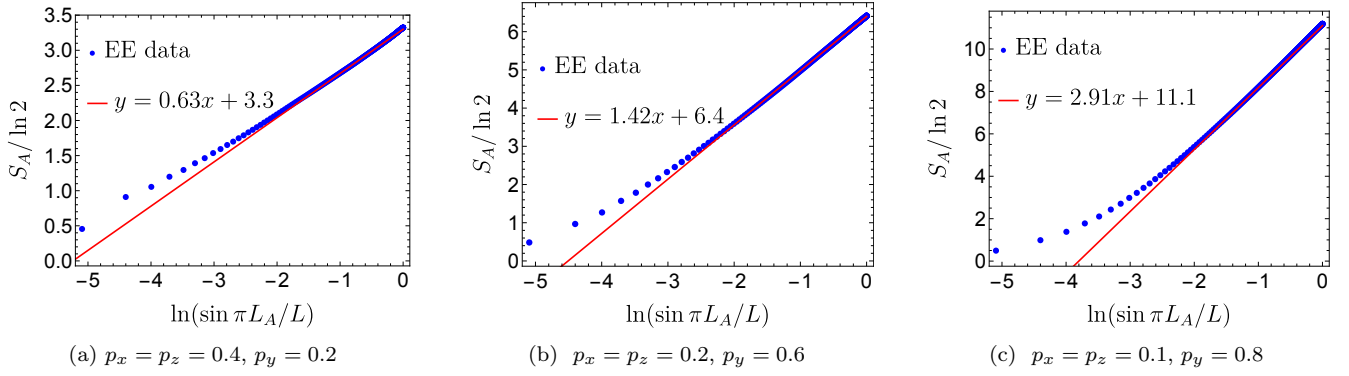
FIG. 20. Logarithmic scaling of entanglement entropy in Goldstone phase with system size $L = 512$
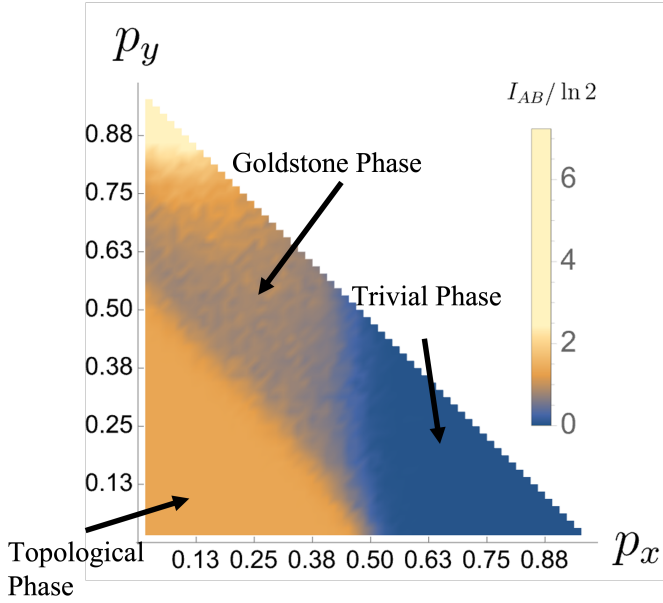

FIG. 21. Phase Diagram of the area-law-area-law model.

This numerical exploration accentuates the fundamental connection between boundary entanglement structure and the computational complexity inherent in Ising models. Such a connection implies that the nature of the entanglement scaling dictates the feasibility of efficient classical approximations of Ising models with complex parameters. Precisely, the volumetric scaling characterizing the entanglement phase transition aligns with the challenges of evaluating the corresponding two-dimensional Ising partition function, while the area-law scaling heralds a phase in which such evaluations become tractable classically.

Our study has enriched our comprehension of the interplay between boundary entanglement scaling and computational complexity. The analytical understanding of the volume-law-area-law boundary entanglement transition induced by bulk measurement is still vacant; it would be interesting to utilize the connection between the Ising partition function and the boundary state to understand the boundary entanglement phase transition analytically.

We observe various entanglement phase transitions on the 1d boundary state induced by bulk measurement. Varying the measurement angle on the Bloch sphere and the measurement rate of random Pauli measurement, we observe entanglement phase transition on the boundary.

ACKNOWLEDGMENTS

[1] Y. Li, X. Chen, and M. P. Fisher, Measurement-driven entanglement transition in hybrid quantum circuits, Physical Review B **100**, 134306 (2019).

[2] B. Skinner, J. Ruhman, and A. Nahum, Measurement-induced phase transitions in the dynamics of entanglement, Physical Review X **9**, 031009 (2019).

[3] S. Sang, Y. Li, T. Zhou, X. Chen, T. H. Hsieh, and M. P. Fisher, Entanglement negativity at measurement-induced criticality, PRX Quantum **2**, 030313 (2021).

[4] J. C. Hoke, M. Ippoliti, D. Abanin, R. Acharya, M. Ansmann, F. Arute, K. Arya, A. Asfaw, J. Atalaya, J. C. Bardin, A. Bengtsson, G. Bortoli, A. Bourassa, J. Bovaird, L. Brill, M. Broughton, B. B. Buckley, D. A. Buell, T. Burger, B. Burkett, N. Bushnell, Z. Chen, B. Chiaro, D. Chik, C. Chou, J. Cogan, R. Collins, P. Conner, W. Courtney, A. L. Crook, B. Curtin, A. G. Dau, D. M. Debroy, A. D. T. Barba, S. Demura, A. D. Paolo, I. K. Drozdov, A. Dunsworth, D. Eppens, C. Er-

ickson, L. Faoro, E. Farhi, R. Fatem, V. S. Ferreira, L. F. Burgos, E. Forati, A. G. Fowler, B. Foxen, W. Giang, C. Gidney, D. Gilboa, M. Giustina, R. Gosula, J. A. Gross, S. Habegger, M. C. Hamilton, M. Hansen, M. P. Harrigan, S. D. Harrington, P. Heu, M. R. Hoffmann, S. Hong, T. Huang, A. Huff, W. J. Huggins, S. V. Isakov, J. Iveland, E. Jeffr, C. Jones, P. Juhas, D. Kafri, K. Kechedzhi, T. Khattar, M. Khezri, M. Kieferová, S. Kim, A. Kitaev, P. V. Klimov, A. R. Klots, A. N. Korotkov, F. Kostritsa, J. M. Kreikebaum, D. Landhuis, P. Laptev, K.-M. Lau, L. Laws, J. Lee, K. W. Lee, Y. D. Lensky, B. J. Lester, A. T. Lill, W. Liu, A. Locharla, F. D. Malone, O. Martin, J. R. McClean, T. McCourt, M. McEwen, K. C. Miao, A. Mieszala, S. Montazeri, A. Morvan, R. Movassagh, W. Mruczkiewicz, M. Neeley, C. Neill, A. Nersisyan, M. Newman, J. H. Ng, A. Nguyen, M. Nguyen, M. Y. Niu, T. E. O'Brien, S. Omonije, A. Opremcak, A. Petukhov, R. Potter, L. P. Pryadko, C. Quintana, C. Rocque, N. C. Rubin, N. S. D. Sank, K. Sankaragomathi, K. J. Satzinger, H. F. Schurkus, C. Schuster, M. J. Shearn, A. Shorter, N. Shutty, V. Shvarts, J. Skruzny, W. C. Smith, R. D. S. G. Sterling, D. Strain, M. Szalay, A. Torres, G. Vidal, B. Villalonga, C. V. Heidweiller, T. White, B. W. K. Woo, C. Xing, Z. J. Yao, P. Yeh, J. Yoo, G. Young, A. Zalcman, Y. Zhang, N. Zhu, N. Zobrist, H. Neven, R. Babbush, D. Bacon, S. Boixo, J. Hilton, E. Lucero, A. Megrant, J. Kelly, Y. Chen, V. Smelyanskiy, X. Mi, V. Khemani, and P. Roushan, Quantum information phases in space-time: measurement-induced entanglement and teleportation on a noisy quantum processor (2023), arXiv:2303.04792 [quant-ph].

[5] Y. Li and M. P. A. Fisher, Statistical mechanics of quantum error correcting codes, Phys. Rev. B **103**, 104306 (2021).

[6] J. C. Napp, R. L. La Placa, A. M. Dalzell, F. G. S. L. Brandão, and A. W. Harrow, Efficient classical simulation of random shallow 2d quantum circuits, Phys. Rev. X **12**, 021021 (2022).

[7] A. Lavasani, Z.-X. Luo, and S. Vijay, Monitored quantum dynamics and the kitaev spin liquid (2022), arXiv:2207.02877 [cond-mat.str-el].

[8] A. Lavasani, Y. Alavirad, and M. Barkeshli, Measurement-induced topological entanglement transitions in symmetric random quantum circuits, Nature Physics **17**, 342 (2021).

[9] A. Lavasani, Y. Alavirad, and M. Barkeshli, Topological order and criticality in $(2 + 1)$D monitored random quantum circuits, Phys. Rev. Lett. **127**, 235701 (2021).

[10] R. Orús, A practical introduction to tensor networks: Matrix product states and projected entangled pair states, Annals of Physics **349**, 117 (2014).

[11] H. Liu, T. Zhou, and X. Chen, Measurement-induced entanglement transition in a two-dimensional shallow circuit, Phys. Rev. B **106**, 144311 (2022).

[12] Y. Bao, M. Block, and E. Altman, Finite time teleportation phase transition in random quantum circuits (2022), arXiv:2110.06963 [quant-ph].

[13] A. P. Lund, M. J. Bremner, and T. C. Ralph, Quantum sampling problems, bosonsampling and quantum supremacy, npj Quantum Information **3**, 15 (2017).

[14] S. Bravyi and R. Raussendorf, Measurement-based quantum computation with the toric code states, Phys. Rev. A **76**, 022304 (2007).

[15] M. Van den Nest, W. Dür, and H. J. Briegel, Completeness of the classical 2d ising model and universal quantum computation, Phys. Rev. Lett. **100**, 110501 (2008).

[16] A. Kitaev, Fault-tolerant quantum computation by anyons, Annals of Physics **303**, 2 (2003).

[17] A.-R. Negari, S. Sahu, and T. H. Hsieh, Measurement-induced phase transitions in the toric code (2023), arXiv:2307.02292 [quant-ph].

[18] J. I. Cirac, D. Pérez-García, N. Schuch, and F. Verstraete, Matrix product states and projected entangled pair states: Concepts, symmetries, theorems, Rev. Mod. Phys. **93**, 045003 (2021).

[19] J. Hauschild and F. Pollmann, Efficient numerical simulations with Tensor Networks: Tensor Network Python (TeNPy), SciPost Phys. Lect. Notes , 5 (2018).

[20] M. Fishman, S. R. White, and E. M. Stoudenmire, The ITensor Software Library for Tensor Network Calculations, SciPost Phys. Codebases , 4 (2022).

[21] M. Fishman, S. R. White, and E. M. Stoudenmire, Codebase release 0.3 for ITensor, SciPost Phys. Codebases , 4 (2022).

[22] A. Nahum, P. Serna, A. M. Somoza, and M. Ortuño, Loop models with crossings, Physical Review B **87**, 10.1103/physrevb.87.184204 (2013).

[23] J. Y. Lee, W. Ji, Z. Bi, and M. Fisher, Measurement-prepared quantum criticality: from ising model to gauge theory, and beyond, arXiv preprint arXiv:2208.11699 (2022).

[24] R. Raussendorf and H. J. Briegel, A one-way quantum computer, Phys. Rev. Lett. **86**, 5188 (2001).

[25] S. Bravyi, D. Gosset, and R. König, Quantum advantage with shallow circuits, Science **362**, 308 (2018), https://www.science.org/doi/pdf/10.1126/science.aar3106.

[26] F. Barahona, On the computational complexity of ising spin glass models, Journal of Physics A: Mathematical and General **15**, 3241 (1982).

[27] K. Fujii and T. Morimae, Commuting quantum circuits and complexity of ising partition functions, New Journal of Physics **19**, 033003 (2017).

[28] S. Istrail, Statistical mechanics, three-dimensionality and np-completeness: I. universality of intracatability for the partition function of the ising model across nonplanar surfaces (extended abstract), in *Proceedings of the Thirty-Second Annual ACM Symposium on Theory of Computing*, STOC '00 (Association for Computing Machinery, New York, NY, USA, 2000) p. 87–96.

[29] H. J. Briegel and R. Raussendorf, Persistent entanglement in arrays of interacting particles, Phys. Rev. Lett. **86**, 910 (2001).

[30] N. Schuch, M. M. Wolf, F. Verstraete, and J. I. Cirac, Entropy scaling and simulability by matrix product states, Phys. Rev. Lett. **100**, 030504 (2008).

[31] G.-Y. Zhu, N. Tantivasadakarn, A. Vishwanath, S. Trebst, and R. Verresen, Nishimori's cat: stable long-range entanglement from finite-depth unitaries and weak measurements (2022), arXiv:2208.11136 [quant-ph].